Journal of Geodynamics 108 (2017) 40–55

Contents lists available at ScienceDirect

Journal of Geodynamics

journal homepage: www.elsevier.com/locate/jog

Grain damage, phase mixing and plate-boundary formation

David Bercovici[a,*], Philip Skemer[b]

[a] Department of Geology & Geophysics, Yale University, New Haven, CT, USA
[b] Department of Earth & Planetary Sciences, Washington University in St. Louis, USA

ARTICLE INFO

Keywords:
Plate tectonics
Mylonites
Damage mechanics

ABSTRACT

The generation of plate tectonics on Earth relies on complex mechanisms for shear localization, as well as for the retention and reactivation of weak zones in the cold ductile lithosphere. Pervasive mylonitization, wherein zones of high deformation coincide with extensive mineral grain size reduction, is an important clue to this process. In that regard, the grain-damage model of lithospheric weakening provides a physical framework for both mylonitization and plate generation, and accounts for the competition between grain size reduction by deformation and damage, and healing by grain growth. Zener pinning at the evolving interface between mineral components, such as olivine and pyroxene, plays a key role in helping drive grains to small mylonitic sizes during deformation, and then retards their growth once deformation ceases. The combined effects of damage and pinning, however, rely on the efficiency of inter-grain mixing between phases (e.g., olivine and pyroxene) and grain dispersal, which likely depends on grain size itself. Here we present a new model for inter-grain mixing and damage and the onset of rapid mixing. The model considers the competition between the formation of new grains behind a receding interphase triple junction (e.g., olivine growing into a boundary between two pyroxene grains) and their severance or spalling during progressive deformation and damage. The newly formed grains of one phase are then transported along the opposing phase's grain-boundaries and the two phases become dispersed at the grain-scale in a growing mixed layer. The small intermixed grains also affect the grain evolution of the surrounding host grains by Zener pinning, and hence influence the rheology and growth of the mixed layer. As the grains in the mixed layer shrink, subsequently spalled new grains are also smaller, causing a feedback that leads to more rapid mixing and shear localization in the mixed layer. The early stages of mixing can be compared to laboratory experiments, but the transition to a steady-state localized mixed layer, as a proxy for a mylonitic zone, can take a few million years at mid lithospheric conditions. Moreover, a transition in mixing efficiency occurs as grain size reduces, which can induce hysteretic behavior, wherein strong, slowly deforming regions can co-exist with weak rapidly deforming zones, analogous to plate tectonic states with large strong plates and narrow weak boundaries.

1. Introduction

The emergence of plate tectonics on Earth, but not other terrestrial planets, remains one of the leading order questions in geoscience today (see Bercovici, 2003; Korenaga, 2013; Bercovici et al., 2015). A distinct feature of plate tectonics is weak localized plate boundaries on which most deformation occurs, separated by large strong and slowly deforming plates. Localized deformation relies on complex rheological mechanisms in addition to the retention and reactivation of weak zones in the cold ductile lithosphere (Gurnis et al., 2000; Bercovici et al., 2015; Bercovici and Ricard, 2014). A significant clue to such behavior exists in the form of mylonites, both in the mantle-lithosphere as well as mid to lower crust (e.g., Etheridge and Wilkie, 1979; White et al., 1980; Jaroslow et al., 1996; Jin et al., 1998; Furusho and Kanagawa, 1999; Montési and Hirth, 2003; Dijkstra et al., 2004; Warren and Hirth, 2006; Skemer et al., 2010; Tasaka et al., 2014; Gueydan et al., 2014; Linckens et al., 2011, 2015; Rahl and Skemer, 2016).

Mylonites are pervasive at many plate boundaries, specifically occurring in zones of high deformation that are characterized by extensive mineral grain reduction (see Bürgmann and Dresen, 2008). The cause for mylonitization, however, is enigmatic. Theories for mylonitization typically treat the coupling of deformation with various possible models of grain size evolution (e.g., see Montési and Hirth, 2003). Grain size evolution is in principle governed by the competition between grain growth or coarsening driven by surface energy minimization (e.g., Hillert, 1965; Karato, 1989; Evans et al., 2001) and grain size reduction driven by deformation, for example, through dynamic recrystallization (Karato et al., 1980; Platt and Behr, 2011). Models of mylonite

* Corresponding author.
E-mail addresses: david.bercovici@yale.edu (D. Bercovici), pskemer@wustl.edu (P. Skemer).

http://dx.doi.org/10.1016/j.jog.2017.05.002
Received 1 December 2016; Received in revised form 22 April 2017; Accepted 20 May 2017
Available online 31 May 2017
0264-3707/

formation in monomineralic or single-phase media (e.g., pure olivine) have been developed using a few approaches. The field-boundary model of De Bresser et al. (2001) proposes that grain size evolves toward the boundary between dislocation and diffusion creep in a deformation-map space (i.e. a stress-grain size space); this occurs because grain size reduction by dynamic recrystallization takes place for relatively large grains in dislocation creep, while only grain-growth is favored for relatively small grains in diffusion creep. Hence, grain sizes are predicted to converge on the boundary between creep regimes, the field boundary, which thus represents a stable dynamic equilibrium.

However, grain sizes typically evolve to the empirically determined stress–grain-size relation called the piezometric line (or paleopiezometer, since it is often used to translate field measurements of grain size into stress), which does not quite coincide with the field boundary (e.g., Van der Wal et al., 1993; Stipp et al., 2010). This piezometric line represents the steady-state balance between grain growth by coarsening, and comminution by dynamic recrystallization; thus this line still resides primarily in the dislocation creep regime. Thus, some models of mylonitization and localization, (e.g., Kameyama et al., 1997; Braun et al., 1999) adopt these empirical relations and stipulate that grain size evolves to a given piezometric line. Other models propose instead a thermodynamic approach in that grain size reduction is driven by damage, wherein deformational work is used to create new surface energy at the grain boundaries, but still by means of dislocations and dynamic recrystallization (Bercovici and Ricard, 2005; Austin and Evans, 2007; Ricard and Bercovici, 2009; Rozel et al., 2011).

However, these monomineralic, single-phase, models, whether empirical or based on damage and thermodynamics, only allow grain size reduction while in dislocation creep, and hence do not permit grain size to shrink into a grain-size-sensitive creep regime, like diffusion creep. Without simultaneous grain-size reduction and grain-size-sensitive creep, there is no positive localization feedback whereby comminution causes weakening, which focuses deformation, which accelerates comminution, and so on. Moreover, mylonites, and especially ultramylonites, typically have grain sizes and other microstructures that are consistent with deformation in the diffusion creep regime, for which the piezometric relations have questionable applicability. The field boundary between diffusion and dislocation creep, therefore, remains a conceptual barrier (as originally stipulated by De Bresser et al., 2001) to these models for explaining mylonites and achieving sufficient plate-tectonic-like localization. Other approaches to break through this barrier have invoked dislocation-accommodated grain-boundary sliding (disGBS) (Hirth and Kohlstedt, 2003; Hansen et al., 2011), which allows for a combination of non-Newtonian behavior with weak grain-size sensitive creep. However, the disGBS mechanism only contributes to deformation over a narrow range of conditions, and cannot account for microstructural evidence for diffusion creep (such as the absence or obliteration of lattice preferred orientation) in natural mylonites and ultramylonites.

Mylonitization, however, is commonly associated with polymineralic rocks, especially in the mantle lithosphere where secondary phases impede grain growth and help hold grain sizes to small values in “permanent diffusion creep” (Warren and Hirth, 2006; Herwegh et al., 2011; Linckens et al., 2011, 2015; Hansen and Warren, 2015). A model for this polymineralic behavior has been proposed using two-phase grain-damage theory (Bercovici and Ricard, 2012), and this provides a physical framework for both mylonitization and plate generation, which is generally consistent with lab and field observations of polycrystalline rocks. In particular, the two-phase grain-damage theory accounts for the competition between damage through deformation, and healing by grain growth, but with the strong influence of Zener pinning by an increase in density of interphase boundary (i.e., the interface between mineral components, such as olivine and pyroxene). Zener pinning in particular helps drive grains to small mylonitic sizes during deformation, where a positive shear-localization feedback exists, and then retards their growth once deformation ceases. Damage to the

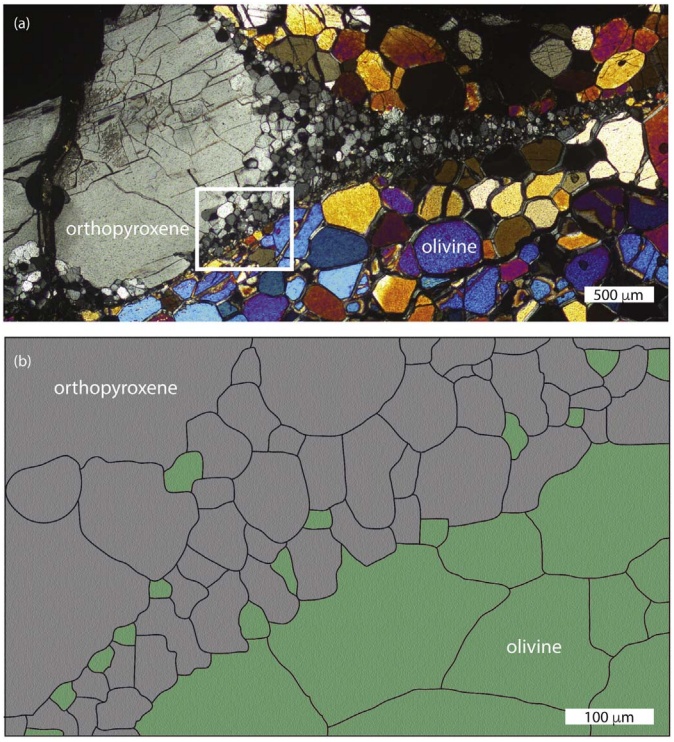

Fig. 1. (a) Petrographic thin section in cross-polarized light of a sheared lherzolite xenolith (from Skemer and Karato, 2008). Olivine and orthopyroxene are dynamically recrystallized, although the recrystallization in orthopyroxene is incomplete. The olivine recrystallized grain size is approximately 5 times larger than the orthopyroxene recrystallized grain size. (b) Line drawing of inset region derived from electron backscatter diffraction (EBSD) mapping (Bruijn and Skemer, 2014). Roughness along the olivine-orthopyroxene interface is correlated with the location of interphase triple junctions. Small olivine grains can be seen along orthopyroxene grain boundaries and within orthopyroxene triple junctions.

interface creates smaller and more effective pinning bodies, and is manifest as interface stirring, rending and inter-grain mixing; indeed the effects of pinning are most pronounced with well dispersed grains. Mixing efficiency, however, likely depends on grain size itself. Recent work even posits that interface damage only becomes efficient at a mixing transition at small grain sizes, which then leads to a hysteresis loop, in which slowly and rapidly deforming states stably coexist, as is characteristic of plate tectonics (Bercovici and Ricard, 2016).

However, the grain-mixing transition itself is a complex process (Linckens et al., 2014; Czertowicz et al., 2016) (see Fig. 1). Although grain-boundary splitting and cavitation are often invoked to account for grain switching (Dimanov et al., 2007; Fusseis et al., 2009; Menegon et al., 2015; Platt, 2015; Viegas et al., 2016; Précigout and Stünitz, 2016), that is likely a low-pressure phenomenon; at mid-lithospheric confining pressures above 1 GPa, which exceed typical rock strength, it is difficult to justify such cavitation. However small amounts of deviatoric tension on grain boundaries can lead to dilation, as material flows into the low pressure zone by viscous creep; this is distinguished from cavitation, in which voids are formed and then filled slowly by diffusion or precipitation from a fluid phase. Here we present a new model for inter-grain mixing and damage, given imposed stress, deformation and grain-boundary dilation, and subsequent feedbacks leading to the onset of rapid mixing.

Our model considers the competition between growth of subgrains into a triple junction (e.g., olivine growing into a pyroxene grain-boundary) and their severance or spalling under deformation and damage. Once the subgrains of one phase are detached into newly formed grains, they are transported along the opposing phases grain-boundaries by pressure gradients induced by both imposed stresses as well as capillary forces, and the phases become dispersed at the grain-scale in a

growing mixed layer. The small intermixed new grains also affect the grain evolution of the surrounding "host" grains by Zener pinning (which generally acts to reduce the host grain size) and hence influence the rheology and growth of the mixed layer. As the grains in the mixed layer become smaller, the spalling new grains also shrink, leading to more rapid mixing and shear localization in the mixed layer. The early stages of mixing can be compared to laboratory experiments (Linckens et al., 2014), although the transition to an eventually steady-state localized mixed layer, as a proxy for a mylonitic zone, may take longer than experiments can be sustained. The formation of mixed mylonitic zones, and ostensibly plate boundaries, likely requires a mixing transition over a finite time, and possibly also leads to hysteretic behavior (Bercovici and Ricard, 2016) with coexisting localized and unlocalized deformation states akin to Earth's plate tectonic environment.

2. Theory

2.1. Olivine teeth

Our model focuses primarily on the interface between two large domains of single phases or components in an overall two-phase mixture; e.g., the inter-phase boundary between large domains of olivine (ol) and pyroxene (px) in a peridotite. (Although the system is not necessarily specific to peridotite, that lithology is appropriate for lithospheric processes; thus we will, for the sake of exposition, henceforth refer to the constitutive phases as olivine and pyroxene.) Both domains are composed of mineral grains and thus the interface between domains has various triple junctions, i.e., where a grain-boundary intersects the interface (see Fig. 2).

Pyroxene, or more specifically orthopyroxene (opx), is observed in both nature and experiments to develop recrystallized grains approximately 5 times smaller than those in olivine under the same deformation conditions (Skemer and Karato, 2008; Linckens et al., 2014). Thus, since pyroxenes typically have smaller grains, we only consider the triple junction of pyroxene grain-boundaries with the interface, and neglect the less frequent triple junctions of olivine grain boundaries with the same interface.

When a new pyroxene grain boundary is formed by subgrain-rotation during dynamic recrystallization, and this grain boundary intersects a phase boundary interface, the triple junction formed at the interface is initially shaped like a "T" (Fig. 2). In olivine and pyroxene, which have similar grain and phase boundary energies, this geometry is unstable. In particular, surface tension or capillary effects causes olivine

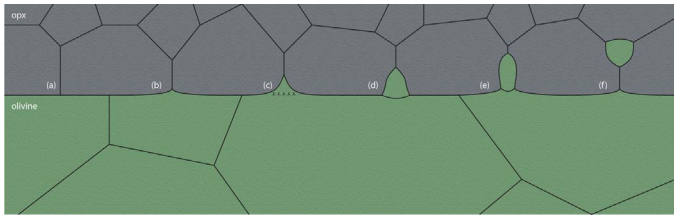

Fig. 2. Schematic cartoon illustrating the sequence of steps described in the present theory. (a) Grain boundaries within adjacent minerals, e.g. olivine (green) and pyroxene (grey), initially intersect the interface or boundary between minerals or phases. (b) Migration of the triple junction introduces roughness along the interphase boundary as a protrusion, which, even without stress and deformation, grows toward the dihedral angle wherein surface energies are balanced. (c) Imposed stress and deformation enhances growth of the protrusion (if there are compressive stresses parallel to the direction along which the protrusion grows); but they also induce damage that promotes dislocations and eventually a subgrain wall behind the migrating protrusion. (d) Deformation increases the misorientation across the subgrain wall leading ultimately to the formation of new grain. (e) With ongoing imposed compressive stresses, the newly formed grain moves along the boundary between two adjacent grains. (f) The grain migrates to a new position that is entirely separate from its parent grain. At this point the process may return to step (b). (For interpretation of the references to color in this figure legend, the reader is referred to the web version of this article.)

to protrude into the triple junctions, and, given time, it would approach the dihedral or wetting angle at which surface tension forces on the junction are in balance (Figs. 2 and 3). However, if the medium is under stress and experiencing deformation, two additional processes can happen. First, normal stresses that are compressional normal to the broad olivine–pyroxene (ol–px) interface, and tensile parallel to the interface, can facilitate the growth of the olivine protrusion or "tooth" (as we'll refer to it, for better or worse, in this paper); in contrast, compression parallel to the ol–px interface will generally impede tooth growth. As these applied stresses tend to be much larger than the wetting forces of surface tension they are more effective in driving mixing.

Second, if there is some component of shear-stress parallel to the interface, then the olivine protrusion or "tooth" develops geometrically necessary dislocations, which form a subgrain boundary at the base of the tooth that evolves into a contiguous grain-boundary. In effect, the olivine "tooth" is damaged or broken off into a new grain, which is subsequently removed and embedded in the pyroxene medium. Wetting forces and normal stresses can further induce a suction force on the dislodged new grain, and transport it along the grain-boundary to the next junction of pyroxene grain-boundaries (Fig. 2). The final size of the tooth (assuming it stops growing – or at best grows very slowly – after it is severed) depends on the competition between how fast it can grow versus how quickly its base accumulates damage during deformation, and is finally severed.

2.1.1. Tooth growth

We first consider the growth of the olivine tooth given a simplified triple junction geometry (Fig. 3). At any given time, the tooth has height (perpendicular to the interface between olivine and pyroxene) y and a base of length $2b$. The base $2b$ has to be less than or equal to the distance between triple junctions, which we equate to the pyroxene grain size R, and thus we assume (and later demonstrate) that $b \propto R$.

The forces driving growth of the tooth include both the effects of wetting by surface tension and suction by applied normal stresses (we neglect the cases where normal stresses impede tooth growth). We seek to translate these forces into pressure gradients that then drive tooth growth via viscous flow (more specifically diffusion creep) into the pyroxene grain-boundary.

We represent the two-dimensional stress tensor in terms of normal and shear components as

$$\underline{\boldsymbol{\tau}} = \begin{bmatrix} \tau_N & \tau_S \\ \tau_S & -\tau_N \end{bmatrix} \equiv \tau_N(\hat{\mathbf{x}}\hat{\mathbf{x}} - \hat{\mathbf{z}}\hat{\mathbf{z}}) + \tau_S(\hat{\mathbf{x}}\hat{\mathbf{z}} + \hat{\mathbf{z}}\hat{\mathbf{x}}) \tag{1}$$

where $\hat{\mathbf{x}}$ and $\hat{\mathbf{z}}$ are unit vectors, respectively parallel and perpendicular to the originally flat interface between phases. Continuity of normal stress on the sloping sides of the tooth implies that the pressure adjacent to these surfaces inside the tooth is $p_\pm = P_0 - \hat{\mathbf{n}}_\pm \cdot \underline{\boldsymbol{\tau}} \cdot \hat{\mathbf{n}}_\pm$, where P_0 is the background pressure,

$$\hat{\mathbf{n}}_\pm = \pm\,\hat{\mathbf{x}}\cos\theta + \hat{\mathbf{z}}\sin\theta \tag{2}$$

is the unit normal to the sloped surface, 2θ is the triple-junction angle, and the $\pm$ represents the right and left surfaces, respectively (Fig. 3). We assume the tooth pressure caused by the imposed stress is the average of these two pressures at these boundaries, and is thus simply $p_t = P_0 - \tau_N(\cos^2\theta - \sin^2\theta)$. The applied stress on the grain-boundary above the tooth acts to pull it open, and likewise induces a pressure $p_{gb} = P_0 - \hat{\mathbf{x}} \cdot \underline{\boldsymbol{\tau}} \cdot \hat{\mathbf{x}} = P_0 - \tau_N$. A vertical pressure gradient thus exists in the tooth and is given by

$$\frac{dp_t}{dz} \approx \frac{p_{gb} - p_t}{y} = -\frac{2\tau_N \sin^2\theta}{y} \tag{3}$$

where we assume the tooth height y is also the basic scale over which pressure changes vertically.

The net surface tension force pulling up on the triple-junction corner of the tooth is $F = (\gamma_1 - 2\gamma_I \cos\theta)L$, where γ_I is the tension at the

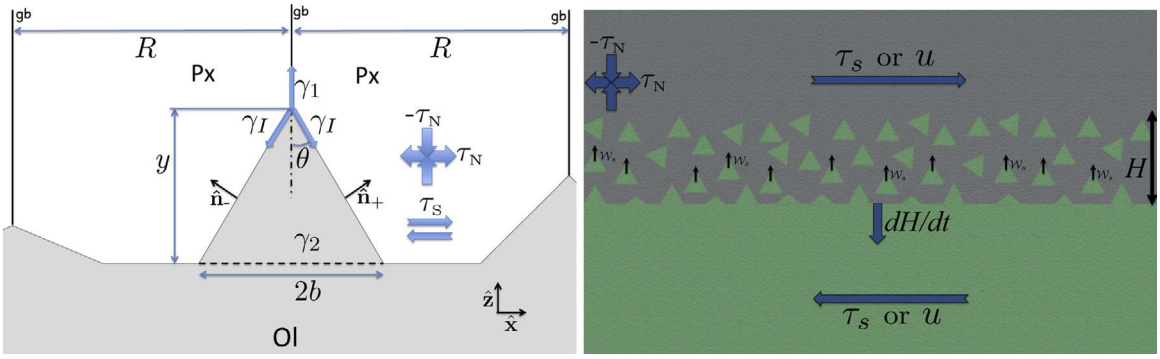

Fig. 3. Left frame: Sketch of olivine "tooth" geometry and surface forces; see text Section 2.1.1 for further discussion. Right frame: Sketch of mixed layer as olivine layer recedes at rate dH/dt while teeth grow and are shorn off during deformation and damage under an imposed shear stress τ_S or velocity filed u (but with the normal stress load τ_N applied in either case).

interface between olivine and pyroxene, γ_1 is the surface tension between pyroxene grains (Fig. 3) and L is the length along the top triple junction into the plane. (Note that we identify phase 1 with pyroxene, and phase 2 with olivine.) This force F goes to zero when the dihedral angle $\theta_D = \cos^{-1}(\gamma_1/(2\gamma_I))$ is reached, i.e., if the olivine and pyroxene grains effectively achieve textural equilibrium with each other. To translate this capillary line-force into a pressure we assume it is distributed over some horizontal plane within the tooth, whose area A is a fraction of the tooth's basal area, i.e. $A = 2fbL$, where fy is also the distance from the plane to the apex of the tooth. The pressure on this plane due to the triple-junction capillary force is $p_c = P_0 - F/A = P_0 - (\gamma_1 - 2\gamma_I \cos\theta)/(2fb)$, where the minus sign denotes that, since the capillary force is upward (in tension) for positive F, the pressure anomaly will have the opposite sign to F. The pressure gradient is due to the drop in pressure from approximately P_0 at the base of the tooth (where the tooth is in contact with an effective half-space of olivine that is closer to mechanical equilibrium than material within the tooth) to p_c over a height $(1 - f)y$ above the base. The pressure gradient is thus $(p_c - P_0)/[(1 - f)y] \propto [(1 - f)f]^{-1}$. While the choice of f is somewhat arbitrary, to be conservative we choose f that leads to the minimum pressure gradient, i.e., $f = 1/2$; in this case

$$\frac{dp_c}{dz} \approx -2\frac{\gamma_1 - 2\gamma_I \cos\theta}{by} \tag{4}$$

In determining (4) we neglect the capillary forces at the base of the tooth, on the two lower corners; in reality these capillary forces act to smooth those corners and minimize their curvature (i.e., the tooth would not be triangular with basal corners but would adopt an elongate and rounded morphology, as illustrated in Fig. 2). But, for simplicity we assume these lower corner forces simply help anchor the corners against the upward suction on the tooth (since the net surface tension force on these corners is outward from the tooth) and keep the base length b more or less fixed, i.e., a fixed fraction of the pyroxene grain size R (which will itself evolve, as considered below). Thus a fixed b during tooth growth implicitly allows for capillary forces at the base of the tooth. However, when the base of the tooth is severed, this assumed anchoring fails, and the net surface tension effect pulls these basal corners inward and adds to the basal pressure, thus helping squeeze the tooth upward; we will deal with this squeezing effect separately (see below under Section 2.2.3).

The net force due to pressure gradients driving vertical growth of the tooth is the sum of (3) and (4):

$$-\frac{dp}{dz} \approx 2\frac{b\tau_N \sin^2\theta + \gamma_1 - 2\gamma_I \cos\theta}{by} = \frac{\Delta P}{y} \tag{5}$$

This pressure gradient drives flow of olivine into the gap between pyroxene grains, which allows growth of the tooth. We assume the major resistance to this pressure force is viscous channel flow of the olivine tooth itself. Treating the pyroxene channel walls as approximately no-slip, and the channel of mean width b, the movement of olivine material into the gap is approximated by simple Poiseuille flow, and the volume flux (per unit length into the plane) filling the tooth is

$$\dot{V} = \frac{d(yb)}{dt} = \frac{b^3}{12\mu_t}\frac{\Delta P}{y} \tag{6}$$

where μ_t is the viscosity of the tooth.

We assume that the rheology of the tooth is dominated by Newtonian diffusion creep, which we further assume is dependent on a tooth grain size proportional to the tooth width b, because the diffusive flux that permits tooth growth is through a cross-section proportional to b. In this case $\mu_t \approx \tilde{b}^m/(2B_2)$ where $\tilde{b} \propto b$, B_2 is the olivine diffusion creep compliance and $m = 2$ or 3, depending on whether the rheology obeys Nabarro–Herring or Coble creep, respectively (see Table 1); here we generally adopt a value of $m = 3$. (We note that an alternate rheology-controlling grain size could be $\sqrt{yb}$, however this implies the viscosity goes to 0 for $y \to 0$, which is unphysical.)

We also note that the assumption that the tooth squeezes through the grain-boundary gap via diffusion creep is limited to b smaller than

Table 1
Table of material properties.

Definition	Formula	Amplitude (s^{-1})	Act. energy (kJ/mol)	Act. volume (cm^3/mol)	Exponent
Dislocation creep compliance (ol)	$A_2 = A_0(\text{MPa})^{-n} e^{\frac{E_a + PV_a}{RT}}$	$A_0 = 1.1 \times 10^5$	$E_a = 530$	$V_a = 14$	$n = 3$
Dislocation creep compliance (opx)	$A_1 = A_0(\text{MPa})^{-n} e^{\frac{E_a + PV_a}{RT}}$	$A_0 = 6.92 \times 10^8$	$H_a = 600$ (enthalpy only)	n/a	$n = 3$
Diffusion creep compliance (ol, px)	$B = B_0(\mu\text{m})^m e^{\frac{E_b + PV_b}{RT}}$	$B_0 = 1.5 \times 10^3$	$E_b = 375$	$V_b = 6$	$m = 3$
Grain mass transfer rate	$G = G_0(\mu\text{m})^p e^{\frac{E_g + PV_g}{RT}}$	$G_0 = 2 \times 10^4$	$E_g = 300$	$V_g = V_b$	$p = 2$
Damage fraction	$f = f_0 e^{2\left(1 - \left(\frac{T}{1000\,\text{K}}\right)^{2.9}\right)}$	$f_0 = 3 \times 10^{-3}$			

Olivine creep laws from Hirth and Kohlstedt (2003), using $n = 3$ instead of $n = 3.5$. Opx dislocation creep law from Bruijn and Skemer (2014) (see Lawlis, 1998; Bystricky et al., 2016) using $n = 3$ instead of $n = 2.9$. Grain-growth law from Karato (1989) for olivine, using $E_g = 300$ instead of 200. Damage fraction law from Rozel et al. (2011) but using f_0 from Section 4.1.

the olivine field boundary grain size. As discussed above, experiments suggest that by the time the grain mixing process begins, the pyroxene grains have already undergone some reduction by dynamic recrystallization (Skemer and Karato, 2008; Linckens et al., 2014), and thus the pyroxene grain size R is already close to the field boundary between dislocation and diffusion creep regimes for pyroxene (Bruijn and Skemer, 2014). Moreover, the olivine field-boundary grain size is larger than that for pyroxene (at a given stress and temperature), and since $b < R$, the olivine teeth sizes are well below the olivine field boundary and in the diffusion creep regime. Therefore, tooth growth and flow likely proceeds by diffusion creep.

Although b varies with time, it does so in parallel with the evolution of pyroxene grain size R (as discussed below in Section 2.2.1), which we assume is much slower than tooth growth; thus we assume the volume flux $\dot{V}$ is accommodated by growth in tooth height y. Lastly we further assume that all the surface tensions, γ_I, γ_1, as well as γ_2 (the olivine grain-boundary surface energy) are roughly equivalent and denoted by γ. Taking all these assumptions together, (6) leads to

$$\frac{dy}{dt} = \frac{B_2}{3b^{m-1}y}\left(b\tau_N \sin^2\theta + \gamma(1 - 2\cos\theta)\right) \tag{7}$$

2.1.2. Tooth damage and severance

We next assess the damage done to the base of the tooth by the imposed deformational work. In principle, this process involves the accumulation of geometrically necessary dislocations at the base of a subgrain, although here we treat it as a simple thermodynamic, or energy exchange, problem. The system is under stress $\underline{\boldsymbol{\tau}}$ given by (1) which drives motion at velocity $\mathbf{v} = u\hat{\mathbf{x}} + v\hat{\mathbf{z}}$. The rate of work done per unity area on either of the sloping surfaces of the tooth is

$$\hat{\mathbf{n}}_{\pm}\cdot\underline{\boldsymbol{\tau}}\cdot\mathbf{v} = (\pm\tau_N\cos\theta + \tau_S\sin\theta)u + (\pm\tau_S\cos\theta - \tau_N\sin\theta)v \tag{8}$$

The velocity field in the vicinity of the tooth can be written as

$$u = 2\dot{e}_S z + \dot{e}_N x \quad \text{and} \quad v = -\dot{e}_N z \tag{9}$$

where $\dot{e}_S$ is the shear-strain rate parallel to the mean ol–px surface (i.e., along the x-direction), $\dot{e}_N$ is the normal strain-rate, and we define the coordinate origin ($x = 0$, $z = 0$) to be the base of the tooth beneath its apex. The rate of work per area acts on an element of area (per length into the plane) on the sloping tooth surfaces given by $dz/\cos\theta$, and summing up the work done on that element on both sides of the tooth (allowing that $\hat{\mathbf{n}}_+$ occurs for $x > 0$ and $\hat{\mathbf{n}}_-$ is for $x < 0$) gives

$$d\dot{W} = \left(4\tau_S\dot{e}_S z\sin\theta + 2\tau_N\dot{e}_N(|x|\cos\theta + z\sin\theta)\right)\frac{dz}{\cos\theta} \tag{10}$$

We then integrate this work rate from $z = 0$ to $z = y$ and note that along the sloped surfaces $|x| = (y - z)\tan\theta$; in this case we arrive at

$$\dot{W} = 2\tan\theta(\tau_S\dot{e}_S + \tau_N\dot{e}_N)y^2 = 2(\tau_S\dot{e}_S + \tau_N\dot{e}_N)by \equiv \underline{\boldsymbol{\tau}}:\dot{\underline{\mathbf{e}}}\ by = \frac{\tau^2 by}{\mu} \tag{11}$$

where μ is the viscosity of the medium above the mean interface (which is originally pure pyroxene) wherein $\underline{\boldsymbol{\tau}} = 2\mu\dot{\underline{\mathbf{e}}}$; we have also used $\tan\theta = b/y$, and the definitions of the strain-rate tensor

$$\dot{\underline{\mathbf{e}}} = \dot{e}_N(\hat{\mathbf{x}}\hat{\mathbf{x}} - \hat{\mathbf{z}}\hat{\mathbf{z}}) + \dot{e}_S(\hat{\mathbf{x}}\hat{\mathbf{z}} + \hat{\mathbf{z}}\hat{\mathbf{x}}) \tag{12}$$

and the second stress invariant

$$\tau^2 = \frac{1}{2}\underline{\boldsymbol{\tau}}:\underline{\boldsymbol{\tau}} = \tau_N^2 + \tau_S^2 \tag{13}$$

Some fraction f of the deformational work goes into creating a new grain-boundary at the base of the olivine tooth until it is eventually severed, and this growing olivine grain boundary has surface energy γ_2. As the base of the tooth is being damaged, the newly forming grain-boundary has length $2b\cdot\mathscr{W}$ where $\mathscr{W}$ is a dimensionless fraction. The growth of surface energy on this boundary is supplied by the fraction f of deformational work according to

$$\frac{d}{dt}(2\gamma_2 b\mathscr{W}) = f\frac{\tau^2}{\mu}by \tag{14}$$

Allowing the surface tensions on grain-boundaries and interfaces to be the same (and that changes in grain size R and thus b are slow relative to the rate that the tooth's base is damaged) as already assumed above, (14) leads to

$$\frac{d\mathscr{W}}{dt} = \frac{f\tau^2}{2\mu\gamma}y = \frac{f}{2\mu\gamma}(\tau_N^2 + \tau_S^2)y \tag{15}$$

Eqs. (7) and (15) describe the competition between growth of the olivine tooth and the rate that it is severed. (Note that we assume the growth of the tooth is unaffected by the growing new boundary at the base, since as long as olivine is still in contact with olivine there should still be sufficient diffusion of mass to fill in the the growing tooth.) The tooth is entirely severed when $\mathscr{W} = 1$, at which point the height of the tooth is at its maximum value Y. We can, even now, integrate (7) and (15) to find Y; however a few more governing equations are necessary to describe the physics of the system, thus we will return to this problem in Section 2.4.

2.2. Evolution of the mixed layer

2.2.1. Grain evolution

Once the olivine teeth are shorn off and dislodged into the pyroxene layer, they influence the evolution of the pyroxene grain sizes, especially by Zener pinning from the smaller olivine teeth. The grain size of pyroxene in the layer that entrains the dislodged teeth obeys

$$\frac{dR}{dt} = \frac{G}{pR^{p-1}}\left(1 - \mathfrak{c}\phi\frac{R^2}{r^2}\right) \tag{16}$$

The quantity G controls the rate of surface-tension driven diffusive mass transfer between pyroxene grains (Hillert, 1965; Evans et al., 2001; Ricard and Bercovici, 2009); generally this process leads to coarsening or grain-growth, although with large Zener pining pressures, the coarsening can be stopped and in principle reversed. Because of lack of information for pyroxene values of G, we assume it is similar to that for olivine (see Table 1). Amongst the other quantities in (16), p is an exponent (usually $p = 2$), ϕ is the volume fraction of olivine teeth mixed into the pyroxene, $\mathfrak{c} = 0.87$ which arises from an assumed log-normal grain size distribution (see Bercovici and Ricard, 2012, 2013, 2014), the factor in parentheses is the Zener pinning factor and r represents the size of the pinning body or equivalently the radius of curvature of the blocking interface (Bercovici and Ricard, 2012).

For simplicity, we have neglected grain-boundary damage (due to dynamic recrystallization) on pyroxene grains in the mixed layer. First, recrystallization in the unmixed pyroxene is likely largely already complete after a few tens of percent strain, before the mixing of olivine teeth proceeds (e.g., Linckens et al., 2014). Thus further evolution of the pyroxene grains is assumed to be dominated by Zener pinning pressure of olivine teeth altering the surface energy and chemical potential difference between pyroxene grains. Indeed, in the limit of relatively small pinning body sizes r – which is expected for our model provided sufficiently large driving stresses and tooth damage – the full grain-evolution equation (see Bercovici and Ricard, 2012) is dominated by the form given by (16). In particular, for large grains in dislocation creep but for which $R \gg r$, grain-boundary damage is suppressed by the Zener pinning factor, while if the grains are small enough to be in diffusion creep, grain boundary damage (which is prevalent during dislocation creep) also becomes vanishingly small (Rozel et al., 2011; Bercovici and Ricard, 2012). However, when grain size R is large, but r is not $\ll R$, this assumption is weak and the limitations of the model in that case must be considered.

In this model, the olivine teeth are the small dispersed pinning bodies, and we can equate r to the mean size of these teeth; thus for simplicity, given our 2-D model, we write $r^2 = bY$ (i.e., r^2 is the 2-D

volume of the olivine teeth in the same way that R^2 is the 2-D volume of the pyroxene grains). Moreover, the volume fraction ϕ of olivine teeth mixed into the layer can be estimated by considering the volume of N such teeth at the moment they separate; this volume (per length into the page) is simply NbY. The total volume of the layer into which these teeth have protruded is NRY (see Fig. 3), and thus $\phi = b/R$. We assume this volume fraction is essentially fixed and in principle has a maximum size of 1/2 (i.e., in our simple model the base of the tooth $2b$ cannot be bigger than R); although the typical olivine mixture ratio in peridotite is closer to 60%, this is a bulk value, and is perhaps not relevant for specific small-scale mixed layers. In the mixed layer, ϕ could in principle be significantly less than 50%, although for simplicity we will assume $\phi = 1/2$. Therefore, given the relations for r and ϕ, (16) becomes

$$\frac{dR}{dt} = \frac{G}{pR^{p-1}}\left(1 - c\frac{R}{Y}\right) \tag{17}$$

The Zener pinning factor can cause grain-growth to slow down and even reverse. Reversal of grain growth and thus grain size reduction happens, in principle, because the Zener pinning pressure reverses the chemical potential between big and small grains, that would normally drive mass diffusion from small to big grains during coarsening. With the reversed chemical potential, the tendency toward chemical equilibrium is achieved either by mass diffusion from big to small grains, or nucleating smaller grains from the large distorted grains; either way the grain size is reduced.

2.2.2. Mixed layer rheology

Since the pyroxene grain size evolves according to (17), then the rheology of that layer evolves as well. Because the pyroxene layer becomes a mixture of pyroxene with small olivine teeth, the rheology should reflect this mixture. While we can certainly account for the complexity of the mixture's rheology, we make the simplifying assumption that the rheology only depends on the pyroxene response. In particular, since the olivine teeth are dispersed, then the interconnected pyroxene matrix will dominate the rheological response of that layer. Thus, for a given stress τ, we employ a composite rheology of dislocation and diffusion creep for pyroxene given by

$$\underline{\dot{\boldsymbol{\varepsilon}}} = (A_1\tau^{n-1} + B_1/R^m)\underline{\boldsymbol{\tau}} \tag{18}$$

where A_1 and B_1 are the pyroxene dislocation and diffusion creep compliances, and n and m are constant exponents. (Again, we assume $n = m = 3$ for typical dislocation and Coble creep laws; see Table 1 for a list of rheological properties.) Using (18) in the definition of deformational work (11), then (15) becomes

$$\frac{d\mathscr{W}}{dt} = \frac{f}{\gamma}\left(A_1\tau^{n+1} + \frac{B_1\tau^2}{R^m}\right)y \tag{19}$$

where τ is defined in (13).

2.2.3. Growth of the mixed layer

As olivine teeth grow and are severed they migrate into the overlying pyroxene, and form a mixed layer. The growth of this mixed layer is governed by the rate that the pure olivine layer is eroded away by the loss of olivine teeth. As the original olivine–pyroxene (ol–px) boundary recedes away under this erosion, it leaves behind the olivine teeth and the mixed layer thickens (see Fig. 3).

However, the teeth must also propagate away from the ol–px boundary, as is evident in laboratory experiments (Fig. 1; see also Linckens et al., 2014), and leave behind a new ol–px triple junction on which a new tooth nucleates. Our assumed driving mechanism for transporting a tooth along the pyroxene grain-boundary is nearly identical to that which makes the tooth grow in the first place: both capillary forces as well as suction imposed by normal stresses, as represented by the pressure gradient (5). Yet, once the tooth is severed, additional capillary forces act on the base of the tooth. In particular, when $\mathscr{W} = 1$ and $y = Y$, the bottom corners each experience a net (in the x direction) capillary force of $\pm(\gamma_1(1 - \sin\Theta) - \gamma_2)L = \mp\gamma L\sin\Theta$, where $\pm$ indicates the right and left corners respectively, L is the length of the corner edge into the plane, $\Theta = \tan^{-1}(b/Y)$, and again we assume the surface tensions are equal to the same quantity γ. These line forces are both inward into the tooth and impart a normal traction that is roughly distributed over a vertical surface in the bottom half of the tooth of area $YL/2$, and thus cause a basal high pressure anomaly of approximately $2\gamma\sin\Theta/Y = 2\gamma\sin\Theta\tan\Theta/b$; this adds to the pressure gradient (5) to give the separation pressure gradient

$$-\frac{dp}{dz} \approx 2\frac{b\tau_N\sin^2\Theta + \gamma(1 - 2\cos\Theta + \sin\Theta\tan\Theta)}{bY} = \frac{\Delta P_s}{Y} \tag{20}$$

When the tooth is severed, this pressure gradient provides the initial impulse to drive the tooth along the grain boundary at a mean separation velocity $\mathscr{W}_s$, similar to that for the tooth growth given by (7); to wit

$$\mathscr{W}_s = \frac{B_2}{3b^{m-1}Y}(b\tau_N\sin^2\Theta + \gamma(1 - 2\cos\Theta + \sin\Theta\tan\Theta)) \tag{21}$$

Once the tooth is squeezed through the grain-boundary the driving pressure gradient might be mitigated somewhat, but once the tooth reaches the next junction of pyroxene grain-boundaries it is drawn in by strong capillary forces that make it complete the transit away from the receding interface, leaving behind fresh grain-boundary on which a new tooth can form.

If the original olivine layer is of thickness D_o and becomes eroded away by a thickness H, then at any given time the olivine layer is of thickness $D_o - H$. Over a length along the interface Δx, the mass loss (per unit into the plain) is $d(\rho\Delta x(D_o - H)/dt = -\rho\Delta x dH/dt$. The rate that mass is eroded away depends on the number of teeth lost per unit time. Within the segment Δx there are $N = \Delta x/R$ triple junctions at which teeth are growing. At the time of their separation, each of these teeth have a mass (per unit into the plain) of ρbY, and they are dislodged at a velocity $\mathscr{W}_s$. Thus the mass flux from dislodging N teeth is given by $\rho(\Delta x/R)b\mathscr{W}_s$. Since mass must be conserved, the erosion of the interface must balance the mass loss from the flux of teeth and thus $0 = -\rho\Delta x dH/dt + \rho(\Delta x/R)b\mathscr{W}_s$, or

$$\frac{dH}{dt} = \frac{b}{R}\mathscr{W}_s = \frac{\phi B_2}{3b^{m-1}Y}(b\tau_N\sin^2\Theta + \gamma(1 - 2\cos\Theta + \sin\Theta\tan\Theta)) \tag{22}$$

which describes the evolution of the mixed layer, left behind in the wake of the receding olivine–pyroxene interface, and we have used the identity that $b/R = \phi$. Note that in principle the full time derivative dH/dt includes the advection and pinching of the mixed layer boundaries by compressional motion $v = -\dot{e}_N z$, but we leave this effect absorbed into the time derivative for now (or equivalently assume it is a small effect).

2.3. Dimensionless governing equations

The governing equations of the system are (7), (15) (or equivalently (19)), (17) and (22), which describe the growth of the tooth, the damage or severance of the tooth, the evolution of the pyroxene grains (which influence the rheology of material impinging on the teeth) and lastly the growth of the mixed layer, respectively.

For all cases we allow a normal stress $\tau_N > 0$ such that the grain-boundary into which the tooth is growing (and eventually propagating) is in tension. We eventually consider two driving conditions of constant imposed shear stress τ_S and imposed mean shear strain rate (or imposed velocity at a distal boundary). In either case we assume the system is in uniform deformation in the x direction and thus is independent of x (we do not account for any small scale 2-D motion caused by rheological heterogeneity from the small olivine teeth). In this model geometry, the stress is uniform across the layer no matter how many layers there are.

If the stress is imposed and fixed it is both fixed and uniform for all time and thus a constant of the system. If the mean strain-rate is imposed (by velocity boundary conditions) then the stress is still uniform spatially but varies in time.

We nondimensionalize stress by a given stress scale $\overline{\tau}$ such that $\tau_N = \overline{\tau}\tau'_N$, $\tau_S = \overline{\tau}\tau'_S$ and $\tau^2 = \overline{\tau}^2\tau'^2 = \overline{\tau}^2(\tau_N'^2 + \tau_S'^2)$. For the imposed-stress case, $\overline{\tau}$ is related to the stress invariant such that $\overline{\tau}^2 = \tau_N^2 + \tau_S^2$, which leads and $\tau'^2 = \tau_N'^2 + \tau_S'^2 = 1$ for all time. The relative values of τ'_N and τ'_S can vary, but in this scheme, once τ'_N is chosen as an input parameter then it determines $\tau'_S = \sqrt{1 - \tau_N'^2}$. In the imposed mean strain-rate case, $\overline{\tau}^2$ is the initial stress invariant (as we will show later) and $\tau' = 1$ only at time $t = 0$ and evolves thereafter.

We next nondimensionalize all distances R, y, $b = \phi R$, as well as H by the length scale $\overline{R}$, and time by the time scale $\overline{t}$, given by

$$\overline{R} = \left(\frac{B_1}{A_1\overline{\tau}^{n-1}}\right)^{1/m} \quad \text{and} \quad \overline{t} = \frac{3}{A_1\overline{\tau}^n} \equiv \frac{3\overline{R}^m}{B_1\overline{\tau}} \tag{23}$$

where $\overline{R}$ is the pyroxene field-boundary grain size for stress $\overline{\tau}$, i.e., the grain size at the transition between diffusion and dislocation creep (when the creep strain-rates are equal), and $\overline{t}$ is the deformation time scale (basically the inverse of strain-rate, within a factor of 3) at the field boundary. With these nondimensionalizing scales, the dimensionless governing equations become, after dropping all primes on variables,

$$\frac{dy}{dt} = \frac{1}{b^{m-1}y}(b\tau_N\sin^2\theta + \Gamma(1 - 2\cos\theta)) \tag{24}$$

$$\frac{d\mathscr{W}}{dt} = \mathscr{D}y(\tau^{n+1} + \tau^2/R^m) \tag{25}$$

$$\frac{dR}{dt} = \frac{\mathscr{C}}{pR^{p-1}}\left(1 - c\frac{R}{Y}\right) \tag{26}$$

$$\frac{dH}{dt} = \frac{\phi}{b^{m-1}Y}(b\tau_N\sin^2\Theta + \Gamma(1 - 2\cos\Theta + \sin\Theta\tan\Theta)) \tag{27}$$

where

$$\mathscr{D} = \frac{3f\overline{\tau}\overline{R}}{\gamma}, \quad \mathscr{C} = \frac{3G}{A_1\overline{\tau}^n\overline{R}^p}, \quad \text{and} \Gamma = \frac{\gamma}{\overline{\tau}\overline{R}} \tag{28}$$

Again Y is the maximum value of y when $\mathscr{W} = 1$, $b = \phi R$, $\theta = \tan^{-1}(b/y)$ and $\Theta = \tan^{-1}(b/Y)$. (See Table 2 for a summary of dimensionless variables and parameters.) Note that formally the ratio of diffusion creep compliances B_2/B_1 should appear in (24) and (27); however, since there are no laboratory data for opx diffusion creep, we adopt the olivine diffusion creep law for opx, in which case $B_2/B_1 = 1$. Moreover, the diffusive mass transfer rate G is also nominally for opx, but given the paucity of data for opx we again adopt the olivine values (see Table 1).

2.4. Analytical model of tooth-severance

The grain size evolution, rheological response and growth of the mixed layer of olivine embedded in pyroxene depends on the maximum height of the olivine teeth Y at the moment they're severed. This can be obtained just from (24) and (25) if we assume the process of growth, damage and severance of olivine teeth, represented by dy/dt and $d\mathscr{W}/dt$ is much faster than the grain size adjustment in the pyroxene, represented by dR/dt and migration rate of the olivine–pyroxene boundary (dH/dt). This assumption holds provided $\mathscr{C} \ll \mathscr{D}$, which is generally valid (Bercovici and Ricard, 2012, 2016). In this case, we rewrite (25) as

$$\frac{d\mathscr{W}}{dt} = \frac{Q}{b^q}y \tag{29}$$

where $Q/b^q = \mathscr{D}(\tau^{n+1} + \tau^2/R^m)$ is approximately constant, i.e., it is slowly-varying relative to the time-scale for growth and damage of olivine teeth. In this case $d\mathscr{W}/dt$ and $\mathscr{W}$ are assumed only functions of y (over the more rapid time scale of tooth growth) so that $d\mathscr{W}/dt = (d\mathscr{W}/dy)(dy/dt)$ which leads to

$$\frac{d\mathscr{W}}{dy} = \frac{Qb^{m-1-q}y^2}{b\tau_N\sin^2\theta + \Gamma(1 - 2\cos\theta)} \tag{30}$$

This equation can be integrated from $\mathscr{W} = 0$ to 1 and from $y = 0$ to Y; however substituting $y = b\chi$, $Y = bX$, and defining $q = m + 2$, the integral becomes

$$1 = Q\int_0^X \frac{\chi^2 d\chi}{\frac{b\tau_N}{1+\chi^2} + \Gamma\left(1 - \frac{2\chi}{\sqrt{1+\chi^2}}\right)} = \frac{Q}{\Gamma}\int_0^X \frac{\chi^2(1+\chi^2)d\chi}{\beta + 1 + \chi^2 - 2\chi\sqrt{1+\chi^2}} \tag{31}$$

where $\beta = b\tau_N/\Gamma$. The above equations yields a transcendental equation for the normalized maximum tooth size X as a function of Q/Γ and β. However the full solution for X is impractical for use in the remaining evolution equations for R and H. A reasonable approximate solution to X can be obtained by considering some asymptotic limits. First we note that the dimensionless value of τ_N is typically of order unity since applied tension is needed to drive sufficiently fast tooth growth and separation, and b is typically of order unity, though it can drop to $O(10^{-2})$. The nondimensional number Γ however is very small; i.e. since $\overline{\tau} \sim 100$MPa, $\overline{R} \sim 10 - 1000\,\mu$m (depending on temperature), and $\gamma \approx 1$ Pa m, then typically $\Gamma \ll 1$, and thus $\beta \gg 1$ (see Table 2).

In the limit of small Q, i.e., very little applied work to damage the tooth's base, the tooth will grow more freely before being shorn off, and X can be assumed larger than unity provided $\beta \gg 1$ (otherwise if $\beta \approx 0$ then the tooth will just grow to the dihedral angle solution of $X = 1/\sqrt{3}$); in this case (31) is approximately

Table 2
Table of dimensionless quantities.

	Definition	Reference Equation(s)
Variables		
y	*Tooth* height at time t	(24)
Y	Maximum *tooth* height at severance	$Y = y$ when $\mathscr{W} = 1$
$\mathscr{W}$	Damaged fraction of *tooth* base	(25)
R	Phase 1 (pyroxene) grain-size	(26)
R_p	Grain-size R at pinned state	(38) and (39)
H	Height of mixed layer	(27)
b	Width of *tooth* base	$b = \phi R$
θ	Triple junction half-angle at time t	$\theta = \tan^{-1}(b/y)$
Θ	Triple junction half-angle at severence	$\Theta = \tan^{-1}(b/Y)$
τ_S	Shear stress (variable for imposed mean strain-rate)	(46) and (47)
τ	Square-root of stress invariant (variable for imposed mean strain-rate)	$\tau^2 = \tau_N^2 + \tau_S^2$
Parameters		
$\mathscr{D}$	*Tooth* damage number	(25) and (28)
$\mathscr{C}$	Phase 1 (px) grain mass-transfer number	(26) and (28)
Γ	Grain-boundary capillary number	(24) and (28)
τ_N	Imposed normal stress	(24) and (27)
τ_{S0}	Initial shear stress	$\tau_{S0} = \sqrt{1 - \tau_N^2}$
τ_S	Shear stress (constant for imposed stress)	$\tau_S = \tau_{S0}$ for all time t
ϕ	Volume fraction of phase 2 (olivine)	$\phi = 0.5$
c	Grain-size distribution parameter	$c = 0.87$
p	Grain coarsening exponent	(16), $p = 2$
n	Dislocation creep stress exponent	(18), $n = 3$
m	Diffusion creep grain-size exponent	(18), $m = 3$
Substitutions		
Q	$Q = b^{m+2}\mathscr{D}(\tau^{n+1} + \tau^2/R^m)$	(29)–(31)
ξ	$\xi = y/b$	(31)
X	$X = Y/b$	(31)
β	$\beta = b\tau_N/\Gamma$	(31)
Ω	$\Omega = Q/(4b\tau_N)$	(35)
$\mathscr{K}$	$\mathscr{K} = 3\tau_N\phi/(\mathscr{D}c^5)$	(38)

$$1 = \frac{Q}{\Gamma}\int_0^X \frac{\chi^4 d\chi}{\beta - \chi^2} = \frac{Q}{\Gamma}\left[\beta^{3/2}\tanh^{-1}\left(\frac{X}{\sqrt{\beta}}\right) - \beta X - \frac{X^3}{3}\right]$$
$$\approx \frac{Q}{5b\tau_N}X^5\left(1 + \frac{5X^2}{7\beta}\right) \quad (32)$$

where the last expression arises from a 7th order Taylor expansion of the $\tanh^{-1}$ term. Inspection of full solutions to (31) show that the value of X^2/β is small, e.g., since $X = Y/b$ is unlikely to reach values of $O(100)$. Thus a reasonable constraint for X for small Q is that $X \le (5b\tau_N/Q)^{1/5}$; by empirical reasoning (i.e., comparing to the full solutions) a reasonable approximate solution is $X \approx (4b\tau_N/Q)^{1/5}$.

Alternatively, if Q is very large, then X will be very small since the teeth will be shorn off before they grow very far into the pyroxene grain-boundary. In this case (31) becomes

$$1 = \frac{Q}{b\tau_N}\int_0^X \chi^2 d\chi \quad (33)$$

which immediately leads to the approximate solution $X \approx (3b\tau_N/Q)^{1/3}$.

Both asymptotic solutions depend primarily on the quantity $Q/(b\tau_N)$, and only very weakly on Γ (which, for example, slightly reduces the magnitude of the small-Q solution). We can effectively stitch these limits together into one expression

$$X \approx \left(\Omega + \left(\frac{4}{3}\Omega\right)^{5/3}\right)^{-1/5} \quad (34)$$

where we introduce for convenience $\Omega = Q/(4\Gamma\beta) = Q/(4b\tau_N)$. A comparison of (34) to the full solution for (31) (Fig. 4) shows a remarkably good fit provided $\beta \gg 1$.

We also briefly note for completeness that, in the unlikely case of $\beta \ll 1$, a similar approximate solution can be obtained. In the limit of $Q \to 0$, the tooth grows toward a steady-state dihedral angle condition wherein $\chi \to 1/\sqrt{3}$. For $Q \to \infty$, we can assume $\chi \ll 1$ and $X \to (3\Gamma/Q)^{1/3}$. Stitching together these limits leads to the approximate relation $X \approx (3 + (\frac{Q}{3\Gamma})^{2/3})^{-1/2}$. However, we won't be using these solutions since β is typically very large.

In the end, we recover the direct expression for the maximum tooth height Y by making the appropriate substitutions for $Y = bX$, $b = \phi R$ and $Q = b^{m+2}\mathscr{D}(\tau^{n+1} + \tau^2/R^m)$ (using $q = m + 2$) to arrive at

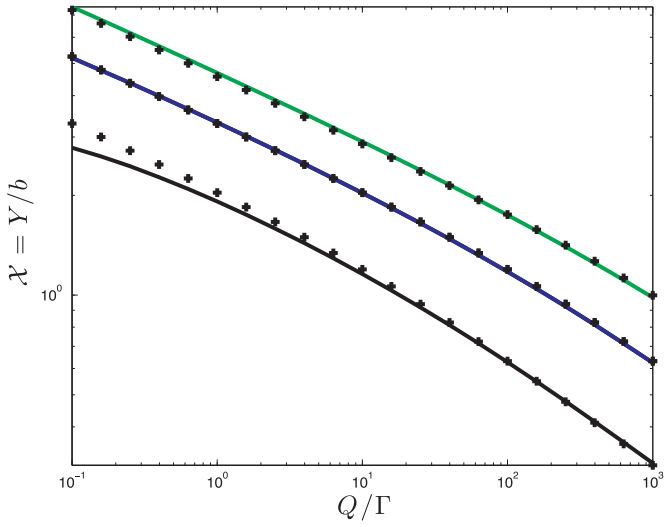

Fig. 4. Maximum "tooth" length Y (normalized by tooth base b) reached before being fully damaged and severed, as a function of Q/Γ, which represents deformational work (see text for discussion). Different curves are for different values of $\beta = 10$ (black), $\beta = 100$ (blue) and $\beta = 500$ (green), using the full numerical solution to (31). Cross symbols represent the analytic approximation (34), which fits well provided $\beta \gg 1$. (For interpretation of the references to color in this figure legend, the reader is referred to the web version of this article.)

$$Y(R) \approx \phi R\left(\Omega + \left(\frac{4}{3}\Omega\right)^{5/3}\right)^{-1/5} \quad \text{where} \quad \Omega(R) = \frac{\mathscr{D}(\phi R)^{m+1}(\tau^{n+1} + \tau^2/R^m)}{4\tau_N} \quad (35)$$

We can then employ this analytic approximate expression for Y in (26) and (27) (although one must account for the analytic expression being most accurate for $\beta = b\tau_N/\Gamma \gg 1$) to obtain the governing evolution equations for the pyroxene grain size R and mixed-layer width H. In fact, the substitution of (35) into the grain-evolution law (26) leads to intriguing predictions suggestive of hysteretic behavior proposed by Bercovici and Ricard (2016); this feature is discussed later in Section 4.3).

3. Some simple applications

3.1. Constant imposed stress

In our assumed geometry, stress τ is uniform across the width of the layer, as already discussed earlier. If stress is imposed and fixed then τ is both uniform and constant in time. This condition would be appropriate if deformation is being driven by an imposed load; e.g., if deformation is driven by a subducting slab and likewise the slab's buoyancy is supported by the viscous resistance of the deformation zone itself. In the next section (Section 3.2) we will consider the case of an imposed mean strain-rate, which has a different interpretation.

Since stress is imposed and fixed then it dictates the stress scale $\bar{\tau}$, in which case the dimensionless stress (square-root of the 2nd invariant) $\tau = 1$, and (35) leads to

$$\Omega = \frac{\mathscr{D}\phi^{m+1}}{4\tau_N}(R^{m+1} + R) \quad (36)$$

where τ_N is still an imposed dimensionless normal stress, albeit $\tau_N \le 1$. Grain size evolution (26) is independent of H and can be integrated directly to obtain $R(t)$, from which we can then also integrate (27) to get $H(t)$, as well as the strain-rate $\dot{e} = 1 + R^{-m}$ in the mixed layer (Fig. 5). These calculations typically show an initially gradual reduction in grain size R, because of increasing Zener pinning pressure as more and ever smaller olivine teeth are mixed into the pyroxene, which is then followed by an abrupt drop to a small steady-state grain size. This steady state delineates a pinned-state in which the mixed layer is akin to a mylonite layer with small grains locked in permanent diffusion creep. The mixed layer width likewise grows very slowly during the initial phase of slow grain-reduction, but once the steady pinned state is reached it grows rapidly. Finally, the strain-rate also remains small initially until the transition to mixing occurs, and then it jumps abruptly to large values, indicated large shear localization on the mixed "mylonite" layer.

3.1.1. Steady state grain size and the pinned state

The grain size in this simple model is predicted to go from its initial state $R = R_0$ to a steady state smaller value of $R = R_p$ in a finite time; this final value is the pinned state grain size (hence the subscript p). We can estimate this final grain size R_p and the time it takes to reach it. First, according to (26), $dR/dt = 0$ when $R = Y/\mathfrak{c}$, which, using (35), leads to $\Omega + (\frac{4}{3}\Omega)^{5/3} = (\phi/\mathfrak{c})^5$; this can be recast as a simple polynomial

$$Z^5 + \frac{3}{4}Z^3 - (\phi/\mathfrak{c})^5 = 0 \quad (37)$$

where $\Omega = \frac{3}{4}Z^3$, and which has just one real solution for $\phi = 0.5$ and $\mathfrak{c} = 0.87$ of $Z = 0.41$. An approximate analytic solution is $Z = (\phi/\mathfrak{c})^{5/3}$ (since the polynomial requires $Z < (\frac{4}{3}(\phi/\mathfrak{c})^5)^{1/3}$), which for the same ϕ and $\mathfrak{c}$ gives $Z = 0.40$. The steady pinned-state value of Ω is thus $\frac{3}{4}(\phi/\mathfrak{c})^5$ which, using (36) leads to a polynomial equation (using $m = 3$)

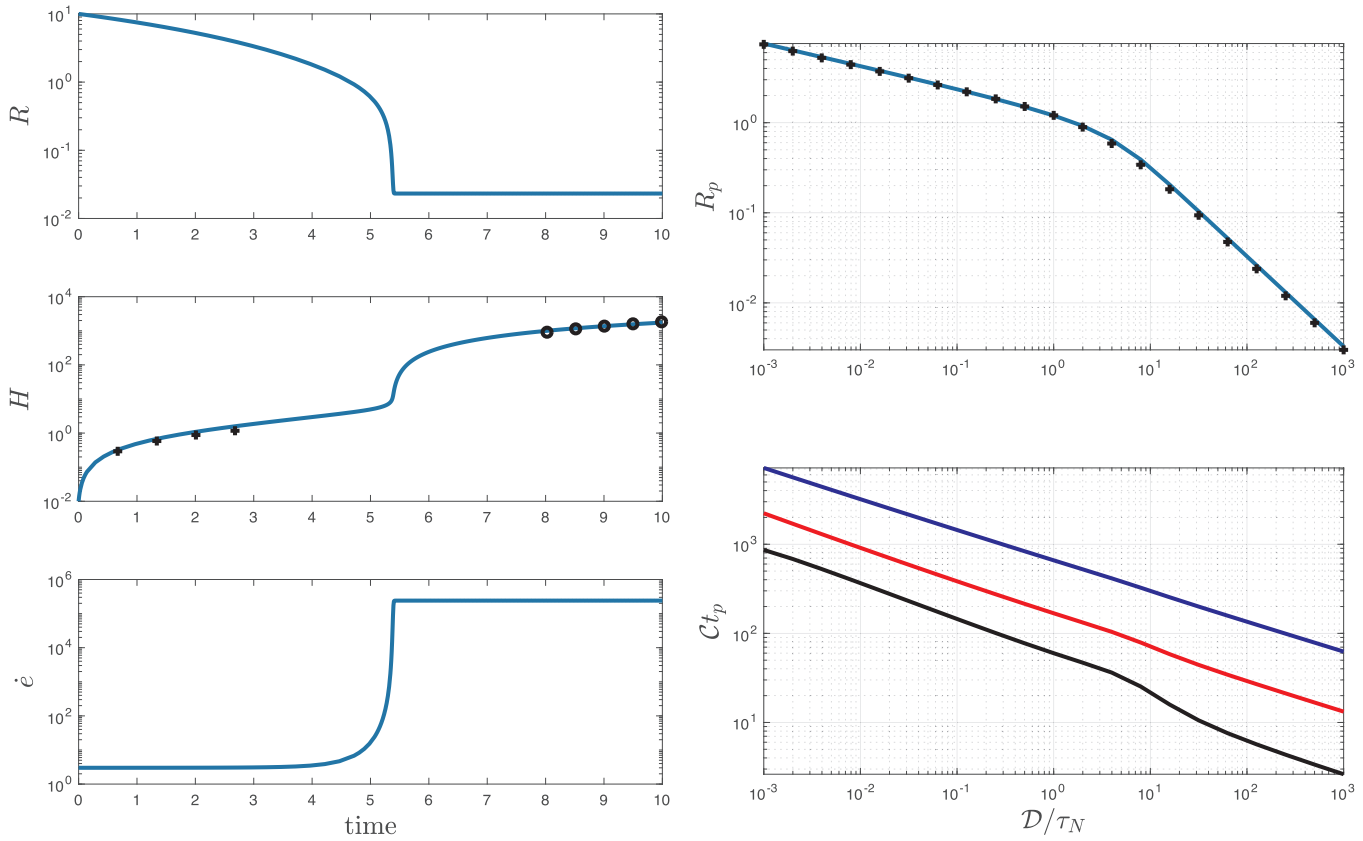

Fig. 5. Left column: A sample evolution for grain-size R, thickness H and strain-rate $\dot{e}$ of the mixed layer for constant imposed stress, with $\mathscr{C} = 1$, $\mathscr{D} = 100$, $\phi = 0.5$, $p = 2$, $m = 3$, $\tau_N = 1/\sqrt{2}$ (so that $\tau_S = \tau_N$) and an initial dimensionless grain-size $R_0 = 10$ (10 times larger than the field-boundary grain-size); symbols on the plot of H are from the approximate initial and final growth rates from (41) and (42). Right column: The steady-state pinned-state grain-size $R = R_p$ (from the solution of (38) with the approximate solution from (39) shown in symbols), and the time to reach this pinned state t_p (from the solution to (40)) versus $\mathscr{D}/\tau_N$. The pinning time is scaled by $\mathscr{C}$, and the colored lines represent different values of initial grainsize, namely $R_0 = 10$ (black), $R_0 = 100$ (red) and $R_0 = 1000$ (blue). Note that (40) cannot be integrated to exactly $R = R_p$, which marks a singularity; thus we integrate to a value of R slightly larger than R_p, for example to $R = 1.001R_p$. (For interpretation of the references to color in this figure legend, the reader is referred to the web version of this article.)

$$R^4 + R - \mathscr{K} = 0 \quad \text{where} \quad \mathscr{K} = \frac{3\tau_N \phi}{\mathscr{D}\mathfrak{c}^5} \tag{38}$$

for which there is one real solution, yielding the value of R_p. A good approximate solution that stitches the asymptotic solutions for large and small R – associated with large and small values of $\mathscr{K}$, respectively – is given by

$$R_p \approx \sqrt{\frac{\mathscr{K}^2}{1 + \mathscr{K}^{3/2}}} \tag{39}$$

which compares favorably to the actual solution for R_p (Fig. 5).

Finally, the time t_p to reach the steady pinned state is given by integrating (26) with (35) and (36), from $R = R_0$ to R_p; this leads to

$$\mathscr{C}t_p = \int_{R_0}^{R_p} \frac{\mathrm{p}R^{p-1}\mathrm{d}R}{1 - \mathfrak{c}R/Y(\Omega(R))} = \Phi(\mathscr{D}/\tau_N, R_0) \tag{40}$$

i.e., t_p, scaled by $\mathscr{C}$ is only a function of $\mathscr{D}/\tau_N$ and R_0, assuming other parameters like ϕ, p, and $\mathfrak{c}$ are well constrained (Fig. 5). (Note that (40) is singular for the exact limit of $R = R_p$, and thus we instead integrate to $R = 1.001R_p$, although the precise choice matters little provided we integrate to just slightly larger than R_p. Moreover, the imprecision of the approximate solution (39) can lead to a singular integral – if the approximation is slightly smaller than the actual R_p– in which case it's necessary to find a precise value of R_p from the complete solution to (37) for Ω, which is then used to find an exact solution to (36).)

3.1.2. Growth of the mixed layer before and during the pinned state

Before the pinned state is reached, the mixed layer thickness H grows slowly; but once the minimum grain size is reached at $t = t_p$, mixing becomes much more efficient and the mixed layer grows rapidly. The initial slow growth of H can be estimated by using (27) and (35), while assuming $R \approx R_0 > 1$, $\Gamma \ll 1$ and $\mathscr{D}/\tau_N \gg 1$, which leads to

$$\frac{\mathrm{d}H_0}{\mathrm{d}t} \approx \left(\frac{\phi\tau_N^2 \mathscr{D}}{3R_0^2}\right)^{1/3} \tag{41}$$

In contrast, the final rapid growth of H once $t = t_p$ and $R = R_p$ can be estimated as well from (27) and (35), under the same parameter ranges, but using the pinned-state condition that $Y = \mathfrak{c}R_p$ along with (39); this leads to

$$\frac{\mathrm{d}H_p}{\mathrm{d}t} \approx \frac{\phi^2\tau_N(1 + \mathscr{K}^{3/2})}{\mathfrak{c}(\mathfrak{c}^2 + \phi^2)\mathscr{K}^2} \sim \mathscr{D}^2/\tau_N \tag{42}$$

These approximate growth rates can be compared to the full numerical integration of (27) (Fig. 5). But these simple relationships demonstrate that growth before $t = t_p$ is a weak function of the damage parameter $\mathscr{D}$ and after $t = t_p$ is a much stronger function of $\mathscr{D}$.

3.2. Constant imposed mean strain-rate

We next consider the case of a constant imposed mean strain-rate in simple shear, which occurs with no-slip constant velocity boundary conditions. This case is relevant for shear deformation being driven by plate motion whose velocity is dictated elsewhere (e.g., by the balance of slab buoyancy with mantle drag).

The specific model geometry (Fig. 6) is such that the mixed layer (of varying grain size $R(t)$, and viscosity $\mu(t)$ and thickness $H(t)$) is sandwiched between an upper layer of pure pyroxene (with grain size R_1, viscosity μ_1 and thickness $D - D_o$) and a receding layer of pure olivine, with grain size R_2, viscosity μ_2 and thickness $D_o - H$. For the moment

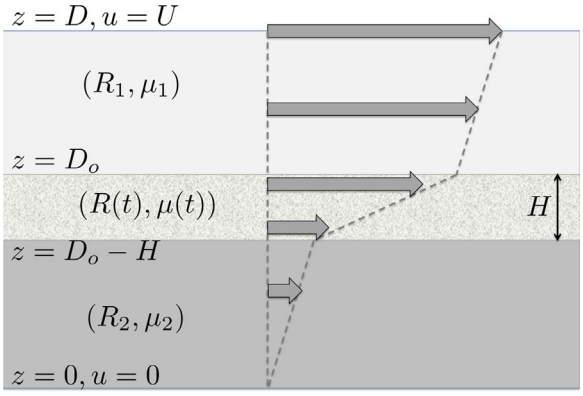

Fig. 6. Geometry for the constant mean strain-rate case, where a constant horizontal velocity $u = U$ is imposed at the upper boundary $z = D$, and $u = 0$ at $z = 0$. The stress is uniform across the layer but changes with time. The local strain rate is variable with depth, but the mean strain rate is always fixed at U/(2D). The variation of stress and local strain-rate with time occurs as the mixed layer, between $z = D_o$ and $z = D_o - H$, thickness and changes mean grain-size R and viscosity μ. The properties of the unmixed layers of pyroxene and olivine (subscripts 1 and 2, respectively) do not change with time, although their thicknesses change.

all properties are dimensional again, until we determine an appropriate stress scale $\bar{\tau}$. Note that while we still have an imposed uniaxial normal stress τ_N, it remains fixed and uniform; we also assume squeezing of the domain vertically is negligible.

Applying the boundary conditions that $u = U$ on the upper boundary adjacent to the peridotite layer, $u = 0$ at the lower boundary adjacent to the olivine layer, that velocities must match with the mixed layer, and that the shear stress τ_S is uniform across the layer, we eventually obtain

$$U = \tau_S\left(\frac{D_o - H}{\mu_2} + \frac{D - D_o}{\mu_1} + \frac{H}{\mu}\right) \tag{43}$$

We assume for simplicity that $\mu_2 \approx \mu_1$, and that μ_1 is given by the rheological law (18) for the strain-rate $\dot{e}$ with the initial pyroxene grain size R_0 (i.e., $\mu_1 = \tau/(2\dot{e})$). Likewise the mixed layer viscosity μ is also given by (18) with the varying grain size $R(t)$. In this case (43) becomes

$$U = 2\tau_S\left(A\tau^{n-1}D + B\left(\frac{D - H}{R_0^m} + \frac{H}{R^m}\right)\right) \tag{44}$$

where A and B are the creep compliances that we have for this case assumed to be the same for the phases. At time $t = 0$ the shear stress is τ_{S0}, and $H = 0$ (no mixed layer, yet), which leads to

$$U = 2\tau_{S0}\left(A(\tau_N^2 + \tau_{S0}^2)^{\frac{n-1}{2}}D + B\frac{D}{R_0^m}\right) \tag{45}$$

that is itself a polynomial equation with which to determine the initial shear stress τ_{S0} given a prescribed boundary velocity U, normal stress τ_N and other system properties; for $n = 3$ this becomes a cubic polynomial equation for τ_{S0}. However, we could more easily prescribe τ_{S0} to obtain a boundary velocity U, and this is what we will assume, i.e., that τ_{S0} is known and prescribed. This will allow the results to be more easily compared to the constant stress case in the previous section.

We thus nondimensionalize stress by the stress scale $\bar{\tau} = \sqrt{\tau_N^2 + \tau_{S0}^2}$, and grain sizes and distances by $\bar{R} = [B/(A\bar{\tau}^{n-1})]^{1/m}$ as before. Setting the dimensionless versions of (44) and (45) equal, and assigning $n = 3$, we arrive at a cubic polynomial equation for the dimensionless stress τ_S

$$\tau_{S0}(1 + 1/R_0^m) = \tau_S(\tau_N^2 + \tau_S^2 + 1/R_0^m + \eta H(1/R^m - 1/R_0^m)) \tag{46}$$

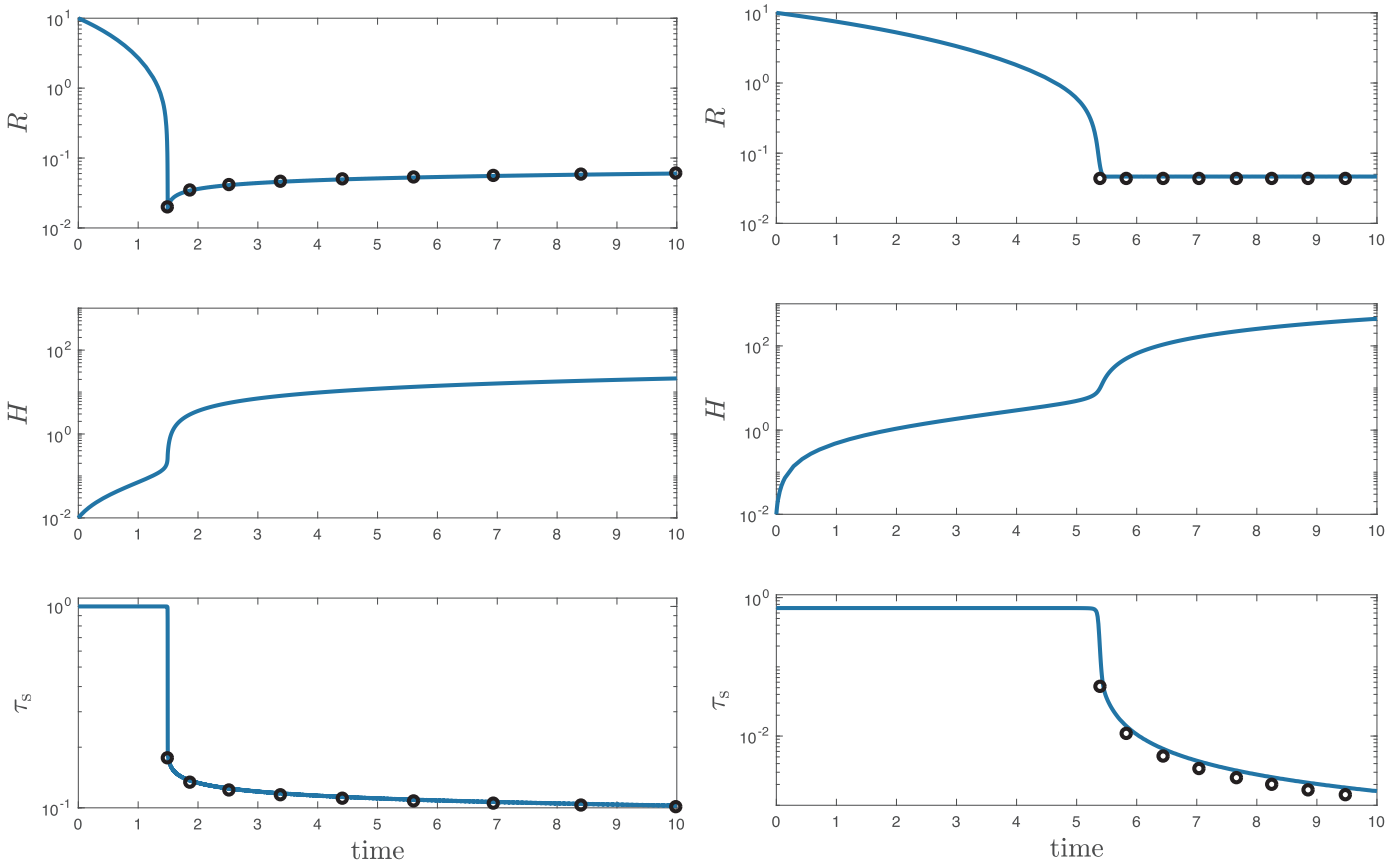

Fig. 7. Sample cases for evolution of grain-size R, thickness H and shear-stress τ_S of the mixed layer for constant imposed mean strain-rate (i.e., imposed velocity boundary conditions), with small normal stress ($\tau_N = 0.02$; left column) and moderately large normal stress ($\tau_N = 1/\sqrt{2}$; right column). In addition $\eta = \bar{R}/D = 10^{-4}$, but all remaining parameters are the same as in Fig. 5. The black-symbols show the approximate quasi-steady state solutions for both limits of τ_N from (50).

where $\eta = \overline{R}/D \ll 1$.

In the initial state when $H = 0$, then $\tau_S = \tau_{S0}$, which is by design. But as $R \to 0$ and H grows (and assuming $R_0^m \gg 1$ and τ_N and τ_S are < 1), then $\tau_S \to \tau_{S0} R^m/(\eta H)$ and thus the shear stress drops to much smaller values than how it started. For intermediate times, stress can be determined as the general solution to (46),

$$\tau_S = E - \frac{b}{3E} \quad \text{where} \quad E = \left(\sqrt{\frac{b^3}{27} + \frac{a^2}{4}} + \frac{a}{2}\right)^{1/3}, \quad a = \tau_{S0}(1 + 1/R_0^m)$$
$$\text{and} b = \tau_N^2 + 1/R_0^m + \eta H (1/R^m - 1/R_0^m) \tag{47}$$

Thus the shear stress τ_S changes with time through the function $b(R, H)$. In the end, the system with imposed mean strain-rate (i.e., velocity boundary conditions) is governed by (26), (27), (35) with (47), again allowing for $\Gamma \ll b\tau_N$. These equations can be integrated, as in the case with constant stress, to understand how the grain size and thickness of the mixed-layer evolves, as well as the stress across the entire medium (Fig. 7). As with the case of fixed stress, grain size R goes to a quasi-steady state value (see next section) in a finite time, and stress drops orders of magnitude in that time also.

3.2.1. Quasi-steady pinned state

The system in constant mean shear-strain-rate is never in a true steady state because the shear-stress τ_S, and hence the grain size R, depend on the mix-layer thickness H, which always grows in time. However, the grain size can enter a quasi-steady state in the pinned limit after which it slowly or barely evolves as the mixed layer grows. In this case we assume $dR/dt \approx 0$, which, as shown in the previous analysis for constant stress, occurs when $R = Y/\mathfrak{c}$, and this leads to $\Omega \approx \frac{3}{4}(\phi/\mathfrak{c})^5$. Using (35) and $n = m = 3$, this results in the simple relation, similar to (38),

$$R^4\tau^4 + R\tau^2 - \mathscr{K} = 0 \tag{48}$$

where $\mathscr{K}$ is defined previously in (38). However, we note that $\tau < 1$ (since it starts with $\tau = 1$ at $t = 0$ and gets smaller as τ_S drops) and that the steady pinned-state grain size R_p is typically very small (i.e, $R_p \ll 1$); in this case we can write $R_p \approx \mathscr{K}/\tau^2$. Substituting this relation for R_p for R in (46) and (while still using $m = 3$) noting that $1/R_0^3 \ll 1, 1/R_p^3 \gg 1$, and that typically $\eta H\tau^4/\mathscr{K}^m \gg 1$ (since typically $\mathscr{K} \ll 1$ and the other factors are not necessarily small) leads to

$$\tau_{S0} = \frac{\eta H}{\mathscr{K}^3}\tau_S\tau^6 \tag{49}$$

which is in principle a 7th order polynomial for τ_S (using $\tau^2 = \tau_S^2 + \tau_N^2$). However rather than solve this equation, we can infer some useful approximate asymptotic relations. In the limit that the normal stress τ_N is not small, say $\tau_N > 1/2$, then $\tau \to \tau_N$ as τ_S drops to very small values in the steady state limit. In contrast, in the limit that $\tau_N \ll 1$, then $\tau \approx \tau_S$. In these two limits of τ_N we find the quasi-steady solutions are well approximated by

$$(R_p, \tau_S) \approx \begin{cases} \left(\frac{\mathscr{K}}{\tau_N^2}, \frac{\tau_{S0}\mathscr{K}^3}{\eta H \tau_N^6}\right) & \text{for } \tau_N > 1/2 \\ \left(\frac{\mathscr{K}}{\tau_S^2}, \left(\frac{\tau_{S0}\mathscr{K}^3}{\eta H}\right)^{\frac{1}{7}}\right) & \text{for } \tau_N \ll 1 \end{cases} \tag{50}$$

which compare favorably (in the right limits of τ_N) to the numerical solutions (Fig. 7). Note that in the limit of non-vanishing τ_N, the pinned-state grain size R_p goes to an actual steady state, while the shear-stress continues to decline as H grows. In the case of very small τ_N, the pinned grain size goes to a quasi-steady state, and τ_S is a weakly decreasing function of H.

3.2.2. Growth of the mixed layer

For constant mean strain-rate, the mixed layer thickness grows considerably more slowly than in the constant stress case. The asymptotic approximations for dH/dt are similar to those shown for the constant stress case, however they are multiplied by powers of τ. In particular, the expression for the initial slow growth of H, is (41) multiplied by $\tau^{4/3}$; and the relation for the final pinned-state rapid growth of H, is effectively (42) multiplied by τ^4. Since τ is a weakly decreasing function of time, this extra factor has little effect on the initial growth of the mixed layer, but τ^4 is a more significantly decreasing function of time and thus more strongly mitigates the final rapid growth of the mixed layer.

Physically, we can interpret this effect in that the appearance of the mixed layer, with its weakening effect that reduces stress, reduces the deformational work going into creating the mixed layer; and thus it limits or slows its own growth. In the constant stress case, the strain-rate increases across the mixed layer, causing it to generate more deformational work and enhance its own growth.

4. Discussion

4.1. Comparison to laboratory experiments

Linckens et al. (2014) performed deformation experiments on peridotitic mixtures of olivine (ol) and orthopyroxene (opx), in which samples containing millimeter-scale grains of olivine and pyroxene were subjected to uniaxial deformation. By design, the interfaces between the olivine and orthopyroxene single crystals were initially smooth. At the end of the experiments, the interface was investigated by secondary electron microscopy (SEM) and electron backscatter diffraction (EBSD). Interface roughness was observed, particularly where recrystallized grain boundaries of opx intersected an olivine grain. The amplitude of this roughness was typically less than one grain diameter. However, in some cases the triple junction was displaced further from the interface and a subgrain boundary was detected behind the migrated triple junction. Linckens et al. (2014) inferred that triple junctions formed in an initially unfavorable "T" shaped configuration, which was relaxed by migration of the triple junction. This migration caused an increase in the roughness of the mineral interface, and perhaps promoted the initial stage of phase mixing. Mixing of olivine grains into the pyroxene was not immediate, but eventually measurable after about 24 h, and with strains of about unity. In that time, olivine grains mixed into the pyroxene layer, but only over distances about 1 or 2 pyroxene grains away from the original ol-opx interface. (Opx grains mixed into the ol layer as well, but the effect was less pronounced.) Although not much mixing occurred in the short available time of the experiments, the results provide some basis for rough comparison and calibration of our model.

The experiments were typically run at high temperatures ($T \leq 1525$ K), modestly high pressures ($P = 1$ GPa) and high stresses ($\tau \approx 500$ MPa) in order to see deformation and some mixing by the end of the experiment. The initial grain size, before deformation proceeded, was approximately 1000 μm. Dynamic recrystallization occurred at relatively small strains (less than the final strain in the experiment), and the recrystallized grain size of the opx was several times smaller than that of the recrystallized ol grains, at the experimental conditions (Linckens et al., 2014, Fig. 4). The typical recrystallized opx grain sizes at the start of mixing were 3–10 μm (see Linckens et al., 2014, Fig. 3 and Table 2).

In order to compare the experiments to our theory we need to scale or nondimensionalize the experimental results. Using the above experimental temperature (the maximum temperature of 1525 K), pressure and stress conditions, and rheological parameters for dislocation creep in opx and diffusion creep in olivine (since diffusion creep data for opx unfortunately does not exist) from various sources (see Table 1), we obtain a nondimensionalizing length scales, from (23), $\overline{R} = [B_1/(A_1\overline{\tau}^{n-1})]^{1/m} = 6.6$ μm,where $\overline{\tau} = 500$ MPa.

The value of $\overline{R}$ is, in principle, the opx field-boundary grain size, and is in fact very close to the mean of the range of the recrystallized

opx grain sizes (3–10 μm). However, the recrystallized grain sizes should reside on the piezometric line, which represents the balance between normal grain-growth and grain comminution by dynamic recrystallization (Austin and Evans, 2007; Rozel et al., 2011). For our given stress and temperature conditions ($\tau = 500$ MPa, $T = 1525$ K), the piezometric opx grain size is approximately 4/3 the grain size on the field boundary (extracted from Bruijn and Skemer, 2014, Fig. 3a), which we would predict to be $\frac{4}{3}\cdot 6.6\ \mu m = 8.8\ \mu m$; this value is well within the observed range of 3–10 μm. Thus we assume the initial nondimensional grain size is $R_0 \approx 4/3$.

The nondimensionalizing time scale, using the opx dislocation creep compliance (again see Table 1) is $3/(A\bar{\tau}^n) = 1.3 \times 10^4$ s. Thus the dimensionless time-span for the experiment (i.e., 24 h) is approximately $t_e \approx 6$.

We can then use the initial growth rate of the mixed layer, approximated by (41), to estimate the conditions for the mixed layer to reach a dimensionless width of $H_e \approx R_0 = 4/3$ in this time span. Assuming equipartitioned normal and shear stresses ($\tau_N = \tau_S = 1/\sqrt{2}$, which makes little difference anyway provided τ_N is of order unity), and $\phi = 0.5$, we can infer that the damage number required to achieve the observed mixing is, from (41),

$$\mathscr{D} = \frac{3R_0^2}{\phi\tau_N^2}\left(\frac{H_e}{t_e}\right)^3 = 2^9/3^7 = 0.23 \tag{51}$$

From (28) this would require a value of the damage partitioning fraction of $f = \gamma D/(3\bar{\tau}\bar{R}) \approx 2.3 \times 10^{-5}$ (where we use $\gamma = 1$). This value of f is in fact rather plausible, given the somewhat sparse constraints on f extracted indirectly from experiment (Austin and Evans, 2007; Rozel et al., 2011). Indeed Rozel et al. (2011) estimated f as a function of T from piezometric data for olivine from various experiments, although to do so they adopted the unusually low grain-growth activation energy of 200 kJ/mol to find, for example, that at $T = 1000$ K, $f \approx 0.1$; this is to be expected since a large damage fraction would be needed to balance rapid grain-growth in order to reach the steady-state piezometric line. Using higher activation energies typical of diffusion of around 300 kJ/mol leads to much slower grain-growth and hence lower damage fractions, e.g., $f \approx O(10^{-3})$ at $T = 1000$ K (see Mulyukova and Bercovici, 2017). To obtain $f = 2.3 \times 10^{-5}$ at $T = 1525$ K would require $f = 3 \times 10^{-3}$ at $T = 1000$ K using the Rozel et al. (2011) relation (see Table 1), which is consistent with estimates for f using the plausible activation energies for diffusion, as well as what we have typically adopted in previous studies (Bercovici and Ricard, 2013, 2014, 2016).

In summary, the observed experimental grain mixing is consistent with the model predictions using plausible available laboratory laws for rheology, grain-growth and damage fraction, although clearly with many unknowns permeating these estimates.

4.2. Scaling and applications to tectonic settings

The theoretical model predicts that the grain size in the mixed layer approaches a steady-state (or quasi-steady-state) size in the pinned limit, wherein the small olivine teeth mixed into the pyroxene dictate grain-evolution primarily via the induced Zener pinning pressure (i.e., to drive the system well into the permanent diffusion creep regime). The mixed layer with this final small-grain size is ostensibly comparable to a mylonite zone, and we can estimate the predicted typical mylonite grain size, the time it takes to reach this steady-state, and the typical width of the mixed layer over geological time scales.

Here we consider the cases for a fixed applied stress, which is a simpler system and whose theoretical results are generally easier to interpret. One can qualitatively expand our inferences to include the fixed mean-strain-rate case. In either case the steady-state pinned grain size R_p is given in dimensionless form by (39), although for the geological cases considered here, the quantity $\mathscr{K}$, given in (38), is small and thus $R_p \approx \mathscr{K}$. When redimensionalized by $\bar{R}$, the pinned grain size is

$$\mathrm{R_p} = R_p\bar{R} = \frac{3\tau_N\phi}{\mathscr{D}\mathfrak{c}^5}\bar{R} = \frac{\gamma\tau_N\phi}{f\bar{\tau}\mathfrak{c}^5} \tag{52}$$

where we have used the definitions of $\bar{R}$ and $\mathscr{D}$ given by (23) and (28). Recall that $\bar{\tau}$ is the applied stress scale and has dimensions of Pa, while τ_N remains a dimensionless normal stress; thus the units of the expression for the pinned grain size are contained in the ratio $\gamma/\bar{\tau}$. The pinned grain size is, accordingly, independent of rheological and grain-growth parameters and their implicit temperature dependence; however, temperature-dependence occurs through the partitioning fraction f, the reference value of which is inferred from the experiments as discussed in the previous section (see Table 1). Physically, (52) shows that the final smallest pyroxene grain sizes depend on the size of the olivine teeth dispersed into the mixed layer; the teeth size depends on the competition between the net applied stress and work acting to essentially break off the teeth (by creating new surface energy along the tooth base), as represented by the factor $\gamma/(f\bar{\tau})$, and the normal stresses τ_N that promote tooth growth.

The time to reach a pinned state can be interpreted as the time to start developing mylonite layers. The dimensionless time to reach the steady pinned state is given by (40), which when redimensionalized by the time-scale $\bar{t}$, given in (23), leads to

$$\mathrm{t_p} = t_p\bar{t} = \frac{\Phi(\mathscr{D}/\tau_N, R_0)}{\mathscr{C}}\bar{t} = \frac{\Phi\bar{R}^p}{G} \tag{53}$$

which is a function of temperature T and applied stress $\bar{\tau}$ through both rheological and grain mass-transfer parameters A_1, B_1 and G, as well as the exponents m, n and p (see Table 1). The pinning time $\mathrm{t_p}$ also depends on the initial dimensionless grain size R_0; assuming that the initial dimensional grain size $\mathrm{R_0}$ is the same for all conditions, then the dimensionless $R_0 = \mathrm{R_0}/\bar{R}$ varies with stress and temperature. In total, the pinned state is reached more quickly (i.e., with smaller $\mathrm{t_p}$) with increasing stress and temperature, both of which decrease the field boundary grain size $\bar{R}$, while increasing temperature also causes faster mass transfer between grains given by G (see Fig. 8).

Once the mylonite layer begins to form after a time $\mathrm{t_p}$, it thickens at a rate given approximately by the growth of the mixed layer after the pinned state is reached, i.e., (42). In dimensional form this layer grows according to

$$\dot{\mathrm{H}}_p = \frac{\phi^2\tau_N(1 + \mathscr{K}^{3/2})}{\mathfrak{c}(\mathfrak{c}^2 + \phi^2)\mathscr{K}^2}\cdot\frac{\bar{R}}{\bar{t}} \tag{54}$$

Thus once the mixed layer begins growing substantively, it grows faster with increasing stress as well as temperature because both effects increase the strain-rate scale (given by the factor $1/\bar{\tau}$; see (23)), which dominates over the associated reduction in the field-boundary grain size $\bar{R}$.

The dimensional pinned grain size $\mathrm{R_p}$ and time to reach the pinned state $\mathrm{t_p}$, are both decreasing functions of applied stress $\bar{\tau}$, but have opposite trends with changing temperature (Fig. 8). The growth rate of the mixed layer $\dot{\mathrm{H}}_p$ increases with both increasing stress and temperature. (For this application we continue to use $\phi = 0.5$ and assign $\tau_N = 1/\sqrt{2}$; neither of these parameters have a strong effect provided they do not become extremely small.)

The pinned grain size $\mathrm{R_p}$ reaches the size of typical ultramylonites, approximately 1–10 μm, for tectonic stresses $\bar{\tau} > 100$ MPa given moderately cool lithospheric temperatures ($T = 1000$–1150 K); however it can take a very long time (typically $\mathrm{t_p} > 100$ Myr or much longer) to reach this state. The thickness of the mixed layer for cooler temperatures also grows slowly, reaching < 1 mm to at most 1 m in a million years. For higher temperature (e.g., $T = 1300$ K), $\mathrm{R_p}$ reaches the size of normal mylonites, $\mathrm{R_p} \approx O(10)$ μm for $\bar{\tau} > 100$ MPa, but can do so relatively quickly, in a time $\mathrm{t_p} < 1$ Myr; in this case the mixed layer can grow rapidly, up to tens of meters in a millions years. In either case, the predicted grain-sizes and width of mylonitic bands are consistent with field observations of peridotitic mylonites (e.g., Warren and Hirth,

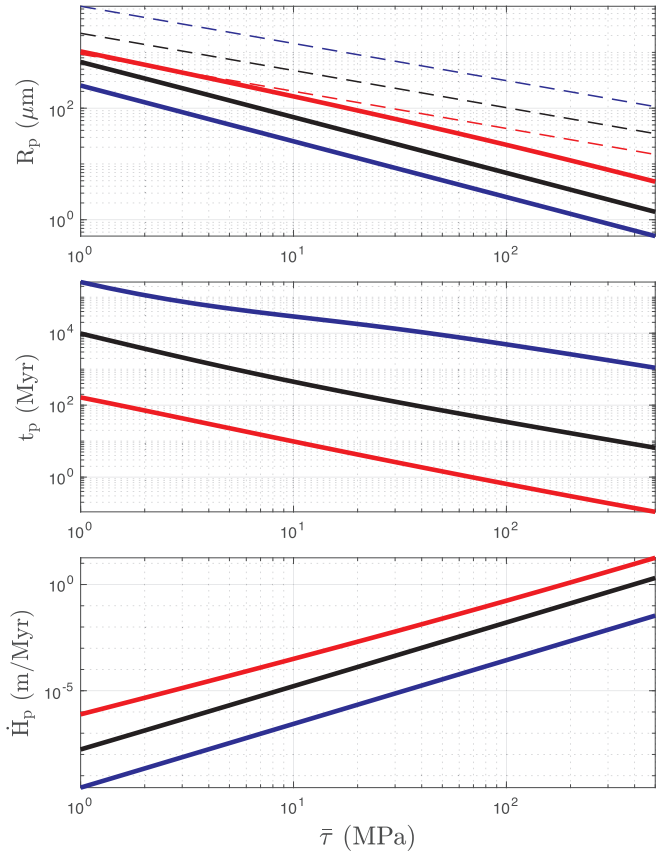

Fig. 8. Pinned-state grain-size R_p, time to reach pinned state t_p, and growth-rate of the mixed layer during the pinned state $\dot{H}_p$, versus applied stress scale $\bar{\tau}$, for the fixed stress cases, but with all quantities dimensionalized using the length and time scales given in (23), as shown in (52–54). The different colored curves are for different lithospheric temperatures, specifically $T = 1000$ K (blue), $T = 1150$ K (black), and $T = 1300$ K (red). The dashed curves on the R_p plot are for the field boundary grain-size $\overline{R}$ (at the indicated temperatures), which is also the dimensionalizing scale, as given by (23). Other parameters used are $\tau_N = 1/\sqrt{2}$ (nondimensional), $p = 2$, $n = m = 3$, $\gamma = 1$ Pa m, $\phi = 0.5$, and lithostatic pressure is assumed to be 2 GPa. The initial grain-size $R_0 = 2000$ μm, which only affects t_p; smaller values of initial grain-size make t_p proportionally small, e.g., a reduction or R_0 by 10 makes t_p about 10 times smaller. See Section 4.2 for further explanation. (For interpretation of the references to color in this figure legend, the reader is referred to the web version of this article.)

2006; Skemer et al., 2010; Linckens et al., 2011, 2015).

In summary, the formation of ultra-mylonite bands at cooler temperatures of 1000 K is sluggish in this model. Although mixing and mixed layer formation are predicted to be much more rapid for warmer temperatures, such temperatures also lead to coarser mylonites. The geological interpretation of this result depends on how quickly mylonite bands develop. If such bands are necessarily generated in a few million years, then this model would predict they can only do so at the warmer temperatures of the lower lithosphere (e.g., $T > 1100$ K). Once the phases and grains are mixed, then dominance of damage over healing (especially given Zener pinning in the mixed layer) becomes more pronounced and leads to more localization and ultramylonite formation, especially if the layer migrates to, or becomes emersed in, cooler temperatures, as, for example, by exhumation or as the lithosphere thickens and cools (see also Braun et al., 1999). At these colder temperatures the rate of healing by grain-growth and interface coarsening is drastically reduced, thus enhancing the longevity of dormant weak zones, which can be inherited to accumulate plate boundaries (e.g., Bercovici and Ricard, 2014).

On Venus, the higher lithospheric temperatures would be more amenable to rapid grain mixing and mixed-layer formation, however, stresses are expected to be as much as an order of magnitude lower than on Earth (Lenardic et al., 2008; Landuyt and Bercovici, 2009; Foley et al., 2012), leading to a commensurate reduction in rate of mixed layer formation. Moreover, if such mixed layers form on Venus, then they would be stuck at high lithospheric temperatures, which then promote faster healing and weaker damage, probably leading to rapid erasure of dormant weak zones.

We should note however that these tectonic interpretations rely on incomplete experimental values for various material properties. For example, diffusion creep laws for pyroxene are unavailable or incomplete at best, and the relation for damage partitioning $f(T)$ is inferred indirectly from the combination of measurements from different experiments, labs and samples (Rozel et al., 2011; Mulyukova and Bercovici, 2017). Thus the precise interpretation of our model results should only be considered with regard to general trends, and taken with a grain of salt (or two).

4.3. Hints of hysteresis

The evolution of pyroxene grain size concurrent with spalling and mixing of olivine teeth, as given by (26) with (35), suggests possible multiple deformation states with hysteretic behavior, wherein strong plates and weak plate boundaries can co-exist, as proposed by Bercovici and Ricard (2016).

The grain-damage theory of Bercovici and Ricard (2012) stipulates that, in a two-phase polymineralic mixture, the damage to the interface between phases reduces the size of Zener-pinning bodies, which help drive grain-reduction into a small-grain “permanent” (i.e., stable) diffusion creep mode characteristic of mylonites, by both retarding grain coarsening (as in standard Zener pinning) and enhancing grain-boundary damage. Bercovici and Ricard (2016) proposed a modification to this theory wherein the efficiency of interface damage increases when grain and pinning body sizes are reduced below a critical value, at which point grain mixing is accelerated (since grain or inter-phase mixing is in itself a manifestation of interface damage). This mixing transition leads to two stable steady states marking the balance of damage and coarsening. One such state involves large grains above the critical grain size, undergoing weak deformation in dislocation creep, which is characteristic of conditions for a paleowattmeter or piezometer relation (i.e., the balance between grain-boundary damage via dynamic recrystallization and normal grain-growth; see Austin and Evans, 2007; Stipp et al., 2010; Rozel et al., 2011). The second stable steady state involves very small grains below the critical size, undergoing strong deformation in diffusion creep, characteristic of mylonites and ultramylonites. A third steady state is unstable and represents an intermediate grain size or a protomylonite state. These three steady-states constitute a hysteresis loop (see Bercovici and Ricard, 2016, Fig. 2) wherein both slowly and rapidly deforming states can stably co-exist for given stress and temperature (or damage and healing) conditions; this is suggestive of the Earth's tectonic environment with both barely-deforming plates and strongly deforming plate boundaries. Here we show that the grain-mixing dynamics of our current model hints at this mixing transition and the multiple deformation states characteristic of hysteresis.

The combination of (26) with (35) by itself predicts only one stable steady state at $R = R_p$, which is the small, pinned-state grain size characteristic of mylonitic conditions (see Section 3.1.1). However, our simple model does not explicitly account for a few effects that could promote background coarsening. First, our model assumes that mixed olivine teeth are always on pyroxene grain-boundaries where they impose a strong Zener pinning pressure that acts to reduce grain size. However, if the pyroxene grains are large enough (relative to the olivine teeth) they can potentially engulf the small olivine teeth, which then become inclusions and cease to exert any pinning pressure; this effect would mitigate Zener pinning and act to restore grain-growth. Second, abnormal grain growth is known to be triggered when secondary phases induce strong pinning, in which case, a small outlier

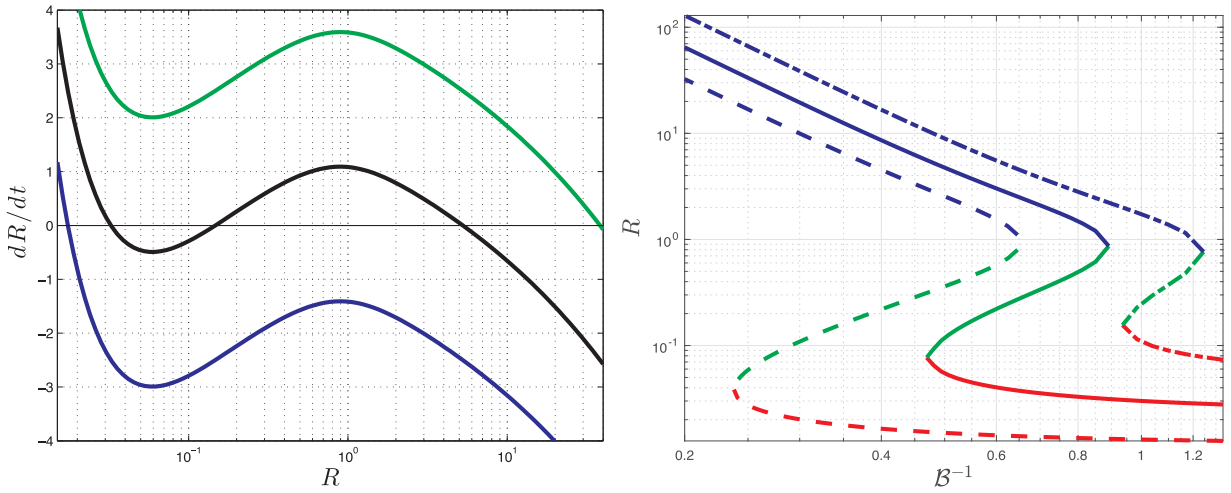

Fig. 9. Left frame: Grain growth rate vs grain size for the model including the possibility of a background coarsening rate, given by (55). Shown are cases for no background growth $\mathscr{B} = 0$ (blue), $\mathscr{B} = 2.5$ (black) and $\mathscr{B} = 5$ (green); all cases have tooth-damage number $\mathscr{D} = 100$. For $\mathscr{B} = 0$ there is one steady solution where $dR/dt = 0$ at a small grain size $R = R_p$. For $\mathscr{B} = 5$ there is one steady solution at large grain sizes. At $\mathscr{B} = 2.5$ there are three steady state solutions, two stable and one unstable. Right frame: Steady-state solutions R to (55) versus $\mathscr{B}^{-1}$, which are, for example, the intersection of the curves in the left panel with $dR/dt = 0$. The three curves shown are for $\mathscr{D} = 200$ (dashed), $\mathscr{D} = 100$ (solid), and $\mathscr{D} = 50$ (dash-dot). Different colors associate with the different steady-states, i.e. large-grain root with $R > 1$ that is stable (blue); the intermediate root with $R < 1$ that is unstable (green) and the small-grain root with $R \ll 1$ (red). All cases shown in both frames are for $\phi = 1/2$, $\tau_N = 1/\sqrt{2}$ and $\mathscr{C} = 1$. (For interpretation of the references to color in this figure legend, the reader is referred to the web version of this article.)

population of large grains can rapidly grow because of Zener pinning pressure placed on the main grain population (Hillert, 1965; Rollett et al., 1989). This effect would also impose a coarsening effect on the mean grain size, although the grain size distribution itself might become bimodal.

In lieu of developing a new model for complexities like engulfment and abnormal growth, we simply assume there is a an added background coarsening effect such that (26) with (35) is recast as

$$\frac{\mathrm{d}R}{\mathrm{d}t} = \frac{\mathscr{C}}{\mathrm{p}R^{p-1}}\left[1 - \frac{\mathrm{c}}{\phi}\left(\Omega + \left(\frac{4}{3}\Omega\right)^{5/3}\right)^{1/5}\right] + \mathscr{B}(R) \quad \text{where} \quad \Omega(R) = \frac{\mathscr{D}}{4\tau_{\mathrm{N}}}(\phi R)^{m+1}\left(1 + \frac{1}{R^m}\right) \tag{55}$$

where $\mathscr{B}$ is an assumed background grain-growth rate, and we have adopted the case for imposed driving stress for which the dimensionless stress invariant $\tau^2 = 1$. For simplicity (and lack of knowledge otherwise) we assume $\mathscr{B}$ is a uniform in R. Eq. (55) is non-monotonic in R and displays extrema, in particular a minimum for $R < 1$, in the diffusion creep regime, and a maximum at $R = 1$ at the field boundary (Fig. 9).

The maximum in (55) at $R = 1$ represents a semi-barrier or region of impedance to grain-reduction, wherein spalling and mixing of small olivine grains is inhibited. This maximum occurs because of enhanced grain reduction on either side of $R = 1$. For $R < 1$, decreasing opx grain size promotes lower viscosity and higher strain-rates (for a given stress) that enhance the damage to the base of the growing olivine teeth, leading to smaller teeth and hence greater Zener pinning pressure, which drives yet faster grain reduction. For $R > 1$, the pyroxene grains are primarily in dislocation creep and tooth damage is independent of grain size (see (25)); however, the olivine teeth grow and flow in diffusion creep and thus become stiffer for larger values of R and tooth base b, thus inhibiting tooth growth, yielding smaller severed teeth, which then also impose greater Zener pinning pressure and faster reduction of the pyroxene grains.

In the case for negligible or no background coarsening (e.g., $\mathscr{B} \approx 0$), we obtain the original cases already discussed earlier, in which tooth damage and mixing drive the system to small grains at the pinned state $R = R_p \ll 1$, which is the only equilibrium point at which $\mathrm{d}R/\mathrm{d}t = 0$ (Fig. 9a, blue curve). For a modest background coarsening (moderately large $\mathscr{B}$) there are three equilibria or steady-state solutions wherein $dR/dt = 0$, at $R > 1$, $R < 1$ and $R \ll 1$ (Fig. 9a, black curve). For significant background coarsening (relatively large $\mathscr{B}$), grain-growth dominates the system except for large grains, and there is only one equilibrium at $R > 1$ (Fig. 9a, green curve). (In principle the equilibrium at $R > 1$ is related to the piezometric or paleowattmeter relations (e.g., Stipp et al., 2010; Austin and Evans, 2007; Rozel et al., 2011); however in this model, the system is only qualitatively representative of this behavior.)

The slope of $\mathrm{d}R/\mathrm{d}t \equiv \dot{R}$ at these equilibria indicates whether they are stable or unstable; i.e., if $\mathrm{d}\dot{R}/\mathrm{d}R < 0$ at an equilibrium point then it is stable, and if $\mathrm{d}\dot{R}/\mathrm{d}R > 0$ then it is unstable. For all cases, the far equilibria at either $R \ll 1$ and $R > 1$ are stable. For modest background coarsening the intermediate equilibrium point at $R < 1$ is unstable.

Thus, in general, for either increasing or decreasing background coarsening $\mathscr{B}$, the steady-state solutions transition from one stable equilibria, to three equilibria (two stable and one unstable), and back to one stable one, characteristic of a hysteresis curve (Fig. 9b), as conjectured by Bercovici and Ricard (2016). These results also support the notion proposed by Bercovici and Ricard (2016) of a mixing transition. For example, for the case of moderate $\mathscr{B}$ and three equilibria, a system with large grains will tend to evolve to the equilibrium at $R > 1$. However if a perturbation allows grain sizes to fall below the unstable intermediate equilibrium at $R < 1$, then the system will evolve to the mylonite-like state at $R \ll 1$. In general, the maximum in $\mathrm{d}R/\mathrm{d}t$, at the field boundary $R = 1$, is a barrier to grain mixing and reduction, but for grain sizes below the barrier, mixing is more effective. This effect also implies that growth of the mixed mylonitic layer would be very slow unless the system could jump this barrier and reach the stable equilibrium at $R \approx R_p \ll 1$, at which point the layer would grow rapidly.

However, some care must be given in interpreting our model in the limit of large pyroxene grains in which $R \gg 1$. First, since the olivine tooth size is dictated by the pyroxene grain size, then at large enough R the teeth could eventually deform by dislocation creep, rather than in grain size-sensitive diffusion creep as we have assumed (see Section 2.1.1). This rheological transition will occur when the tooth base $b = \phi R$ reaches the olivine field boundary grain size, or when $R \approx \phi^{-1}(A_1/A_2)^{1/m} \approx O(10)$, depending on temperature (see Table 1). Thus for $R > O(10)$ our assumption that teeth deform via diffusion creep becomes weak. Moreover, if the olivine teeth can attain sufficiently large sizes when $R > O(10)$ (because they deform in dislocation creep), then our assumption that Zener pinning pressure dominates

pyroxene grain evolution (see Section 2.2.1) becomes weak also, in which case grain-boundary damage (via dynamic recrystallization) would need to be re-introduced. However, our model for pyroxene grain growth, e.g., (55), is only relevant for the mixed layer; in principle, the pyroxene in the adjacent unmixed layer has already undergone grain-reduction by dynamic recrystallization before mixing proceeds, and thus it is unlikely that R would ever be greater than or even close to $O(10)$ in the mixed layer to begin with. Of course, a more comprehensive model would couple grain evolution in the mixed and unmixed pyroxene layers (as well as the olivine layer, which we have neglected entirely, other than its erosion), but we will defer that to future efforts.

5. Summary and conclusion

We have presented a model and analysis of grain evolution and the generation of mylonites, shear localization and tectonic plate boundaries, through mixing and damage in polyphase lithospheric materials. The model considers the mixing of grains of two adjacent layers of homogeneous phases (namely olivine and pyroxene in a lithospheric peridotite) across their common interface while they undergo deformation. There are four coupled processes that lead to simultaneous mixing, grain reduction and shear localization. First, the olivine phase grows protrusions or "teeth" into the adjacent intersecting pyroxene grain-boundaries because of imposed normal stresses as well as capillary forces. Second, the base of the olivine teeth are damaged because of the shear component of stress and deformation, and become severed. Third, the dislodged olivine teeth are squeezed (by the same stress and capillary forces) though the pyroxene grain boundaries to the next grain-boundary triple junctions, and the resulting erosion of teeth causes the original olivine–pyroxene interface to recede, leaving behind a mixed layer of olivine teeth in a host of pyroxene grains. (See Figs. 2 and 3.) Finally, the olivine teeth impose a Zener pinning pressure that drives grain-reduction of the pyroxene grains. These processes couple into a positive feedback: since the pyroxene grain size dictates the olivine tooth size, then as the former reduces so does the latter, causing stronger pinning in the mixed layer, which drives yet smaller grains and teeth, and so on. Moreover, the rate of mixing, growth of the mixed layer and shear localization all accelerate rapidly as the grains and teeth reach their minimum size characteristic of mylonites and ultramylonites.

The results of our model are compared to laboratory experiments, which provide a constraint on the damage process, i.e., the fraction of deformational work that, in this model, goes into creating a new grain-boundary at the base of the olivine teeth. In a geological setting, the model predicts that mixing is very sluggish at mid-lithosphere temperatures around 1000 K. Sufficient mixing occurs at higher, lower-lithospheric temperatures (1100–1300 K) leading to plausible formation of mylonite layers after about 1 Myrs. Lithospheric mixed layers might first be generated at warmer lithospheric depths of the lithosphere; as these regions cool during, for example, sea-floor spreading or exhumation, the pre-mixed zones undergo further damage, while healing and coarsening become more suppressed (and both processes are facilitated by efficient Zener pinning in the mixture; see Bercovici and Ricard, 2012). In the same regard, mixing might also be efficient near deeper lithospheric drips, which would then leave behind a mixed zone to evolve and/or be inherited for later use, such as subduction initiation (e.g., Bercovici and Ricard, 2014). Moreover, this model suggests that mixing was perhaps more efficient in a hotter early Earth, leaving well mixed zones to be inherited for further damage and localization after sufficient planetary cooling.

Finally we note that the coupled physics of grain damage and mixing suggests a hysteretic effect in the grain evolution law that yields co-existing states of deformation, as suggested by Bercovici and Ricard (2016). In particular, because of a grain-mixing transition or barrier, the deforming system can either be in a large-grained, slowly deforming state or a small-grained rapidly deforming state, at the same tectonic conditions (i.e., stress and temperature). This simple model thus predicts that both barely deforming plate interiors and rapidly deforming plate boundaries can coexist for the same tectonic regime, as is evident on Earth.

Acknowledgments

The authors thank Laurent Montési for his thoughtful and thorough review. This work was supported by National Science Foundation Grants EAR-1344538 (for DB) and NSF EAR-1352306 (for PS).

References

Austin, N., Evans, B., 2007. Paleowattmeters: a scaling relation for dynamically recrystallized grain size. Geology 35, 343–346.
Bercovici, D., 2003. The generation of plate tectonics from mantle convection. Earth Planet. Sci. Lett. 205, 107–121.
Bercovici, D., Ricard, Y., 2005. Tectonic plate generation and two-phase damage: void growth versus grainsize reduction. J. Geophys. Res. 110, B03401. http://dx.doi.org/10.1029/2004JB003181.
Bercovici, D., Ricard, Y., 2012. Mechanisms for the generation of plate tectonics by two-phase grain-damage and pinning. Phys. Earth Planet. Int. 202–203, 27–55.
Bercovici, D., Ricard, Y., 2013. Generation of plate tectonics with two-phase grain-damage and pinning: source-sink model and toroidal flow. Earth Planet. Sci. Lett. 365 (0), 275–288.
Bercovici, D., Ricard, Y., 2014. Plate tectonics, damage and inheritance. Nature 508, 513–516.
Bercovici, D., Ricard, Y., 2016. Grain-damage hysteresis and plate-tectonic states. Phys. Earth Planet. Int. 253, 31–47.
Bercovici, D., Tackley, P.J., Ricard, Y., 2015. The generation of plate tectonics from mantle dynamics. In: In: Bercovici (Gerald Schubert editor-in-chief), D. (Ed.), Treatise on Geophysics, 2nd ed., Mantle Dynamics, vol. 7. Elsevier, pp. 271–318 (Chapter 7).
Braun, J., Chéry, J., Poliakov, A., Mainprice, D., Vauchez, A., Tomassi, A., Daignières, M., 1999. A simple parameterization of strain localization in the ductile regime due to grain size reduction: a case study for olivine. J. Geophys. Res.: Solid Earth 104 (B11), 25167–25181. http://dx.doi.org/10.1029/1999JB900214.
Bruijn, R.H., Skemer, P., 2014. Grain-size sensitive rheology of orthopyroxene. Geophys. Res. Lett. 41 (14), 4894–4903. http://dx.doi.org/10.1002/2014GL060607.
Bürgmann, R., Dresen, G., 2008. Rheology of the lower crust and upper mantle: evidence from rock mechanics, geodesy, and field observations. Annu. Rev. Earth Planet. Sci. 36, 531–567.
Bystricky, M., Lawlis, J., Mackwell, S., Heidelbach, F., Raterron, P., 2016. High-temperature deformation of enstatite aggregates. J. Geophys. Res.: Solid Earth 121 (9), 6384–6400. http://dx.doi.org/10.1002/2016JB013011.
Czertowicz, T., Toy, V., Scott, J., 2016. Recrystallisation, phase mixing and strain localisation in peridotite during rapid extrusion of sub-arc mantle lithosphere. J. Struct. Geol. 88, 1–19. http://www.sciencedirect.com/science/article/pii/S0191814116300517.
De Bresser, J., ter Heege, J., Spiers, C., 2001. Grain size reduction by dynamic recrystallization: can it result in major rheological weakening? Int. J. Earth Sci. 90, 28–45.
Dijkstra, A.H., Drury, M.R., Vissers, R.L.M., Newman, J., Van Roermund, H.L.M., 2004. Shear zones in the upper mantle: evidence from alpine- and ophiolite-type peridotite massifs. Geol. Soc., Lond. 224 (1), 11–24. Special Publications, http://sp.lyellcollection.org/content/224/1/11.abstract.
Dimanov, A., Rybacki, E., Wirth, R., Dresen, G., 2007. Creep and strain-dependent microstructures of synthetic anorthite-diopside aggregates. J. Struct. Geol. 29 (6), 1049–1069. http://www.sciencedirect.com/science/article/pii/S0191814107000338.
Etheridge, M., Wilkie, J., 1979. Grainsize reduction, grain boundary sliding and the flow strength of mylonites. Tectonophysics 58 (1-2), 159–178.
Evans, B., Renner, J., Hirth, G., 2001. A few remarks on the kinetics of static grain growth in rocks. Int. J. Earth Sci. (Geol. Rundsch.) 90, 88–103.
Foley, B.J., Bercovici, D., Landuyt, W., 2012. The conditions for plate tectonics on super-earths: Inferences from convection models with damage. Earth Planet. Sci. Lett. 331-332, 281–290.
Furusho, M., Kanagawa, K., 1999. Reaction induced strain localization in a lherzolite mylonite from the Hidaka metamorphic belt of central Hokkaido, Japan. Tectonophysics 313, 411–432.
Fusseis, F., Regenauer-Lieb, K., Liu, J., Hough, R.M., De Carlo, F., 2009. Creep cavitation can establish a dynamic granular fluid pump in ductile shear zones. Nature 459 (7249), 974–977. http://dx.doi.org/10.1038/nature08051.
Gueydan, F., Précigout, J., Montési, L.G., 2014. Strain weakening enables continental plate tectonics. Tectonophysics 631 (0), 189–196. Observational and modelling perspectives on the mechanical properties of the lithosphere http://www.sciencedirect.com/science/article/pii/S0040195114000924.
Gurnis, M., Zhong, S., Toth, J., 2000. On the competing roles of fault reactivation and brittle failure in generating plate tectonics from mantle convection. In: In: Richards, M.A., Gordon, R., van der Hilst, R. (Eds.), History and Dynamics of Global Plate Motions, Geophys Monogr. Ser., vol. 121. Am. Geophys. Union, Washington, DC, pp.

73–94.
Hansen, L.N., Warren, J.M., 2015. Quantifying the effect of pyroxene on deformation of peridotite in a natural shear zone. J. Geophys. Res.: Solid Earth 120 (4), 2717–2738. http://dx.doi.org/10.1002/2014JB011584.
Hansen, L.N., Zimmerman, M.E., Kohlstedt, D.L., 2011. Grain boundary sliding in San Carlos olivine: flow law parameters and crystallographic-preferred orientation. J. Geophys. Res.: Solid Earth 116 (B8). http://dx.doi.org/10.1029/2011JB008220.
Herwegh, M., Linckens, J., Ebert, A., Berger, A., Brodhag, S., 2011. The role of second phases for controlling microstructural evolution in polymineralic rocks: a review. J. Struct. Geol. 33 (12), 1728–1750.
Hillert, M., 1965. On the theory of normal and abnormal grain growth. Acta Metall. 13, 227–238.
Hirth, G., Kohlstedt, D., 2003. Rheology of the upper mantle and the mantle wedge: a view from the experimentalists. In: In: Eiler, J. (Ed.), Subduction Factor Monograph, vol. 138. Am. Geophys. Union, Washington, DC, pp. 83–105.
Jaroslow, G., Hirth, G., Dick, H., 1996. Abyssal peridotite mylonites: implications for grain-size sensitive flow and strain localization in the oceanic lithosphere. Tectonophysics 256 (1), 17–37. http://www.sciencedirect.com/science/article/pii/0040195195001638.
Jin, D., Karato, S., Obata, M., 1998. Mechanisms of shear localization in the continental lithosphere: Inference from the deformation microstructures of peridotites from the Ivrea zone, Northwestern Italy. J. Struct. Geol. 20, 195–209.
Kameyama, M., Yuen, D., Fujimoto, H., 1997. The interaction of viscous heating with grain-size dependent rheology in the formation of localized slip zones. Geophys. Res. Lett. 24, 2523–2526.
Karato, S., 1989. Grain growth kinetics in olivine aggregates. Tectonophysics 168, 255–273.
Karato, S., Toriumi, M., Fujii, T., 1980. Dynamic recrystallization of olivine single crystals during high temperature creep. Geophys. Res. Lett. 7, 649–652.
Korenaga, J., 2013. Initiation and evolution of plate tectonics on earth: theories and observations. Ann. Rev. Earth Planet. Sci. 41, 117–151.
Landuyt, W., Bercovici, D., 2009. Variations in planetary convection via the effect of climate on damage. Earth Planet. Sci. Lett. 277, 29–37.
Lawlis, J., 1998. High temperature creep of synthetic olivine-enstatite aggregates (Ph.D. thesis). Penn. State U., Dept. Geosciences, State College, PA.
Lenardic, A., Jellinek, M., Moresi, L.-N., 2008. A climate change induced transition in the tectonic style of a terrestrial planet. Earth Planet. Sci. Lett. 271, 34–42.
Linckens, J., Bruijn, R.H., Skemer, P., 2014. Dynamic recrystallization and phase mixing in experimentally deformed peridotite. Earth Planet. Sci. Lett. 388, 134–142.
Linckens, J., Herwegh, M., Müntener, O., 2015. Small quantity but large effect – how minor phases control strain localization in upper mantle shear zones. Tectonophysics 643 (0), 26–43.
Linckens, J., Herwegh, M., Müntener, O., Mercolli, I., 2011. Evolution of a polymineralic mantle shear zone and the role of second phases in the localization of deformation. J. Geophys. Res. 116 (B06210), 21pp.
Menegon, L., Fusseis, F., Stünitz, H., Xiao, X., 2015. Creep cavitation bands control porosity and fluid flow in lower crustal shear zones. Geology 43 (3), 227–230.
Montési, L., Hirth, G., 2003. Grain size evolution and the rheology of ductile shear zones. From laboratory experiments to postseismic creep. Earth Planet. Sci. Lett. 211, 97–110.
Mulyukova, E., Bercovici, D., 2017. Formation of lithospheric shear zones: Effect of temperature on two-phase grain damage. Phys. Earth Planet. Int.Submitted.
Platt, J., Behr, W., 2011. Grainsize evolution in ductile shear zones: implications for strain localization and the strength of the lithosphere. J. Struct. Geol. 33 (4), 537–550. http://www.sciencedirect.com/science/article/pii/S0191814111000265.
Platt, J.P., 2015. Rheology of two-phase systems: A microphysical and observational approach. J. Struct. Geol. 77, 213–227. http://www.sciencedirect.com/science/article/pii/S0191814115001029.
Précigout, J., Stünitz, H., 2016. Evidence of phase nucleation during olivine diffusion creep: A new perspective for mantle strain localisation. Earth Planet. Sci. Lett. http://www.sciencedirect.com/science/article/pii/S0012821X1630509X.
Rahl, J.M., Skemer, P., 2016. Microstructural evolution and rheology of quartz in a mid-crustal shear zone. Tectonophysics 680, 129–139. http://www.sciencedirect.com/science/article/pii/S0040195116301482.
Ricard, Y., Bercovici, D., 2009. A continuum theory of grain size evolution and damage. J. Geophys. Res. 114, B01204. http://dx.doi.org/10.1029/2007JB005491.
Rollett, A., Srolovitz, D., Anderson, M., 1989. Simulation and theory of abnormal grain growth–anisotropic grain boundary energies and mobilities. Acta Metall. 37 (4), 1227–1240. http://www.sciencedirect.com/science/article/pii/000161608990117X.
Rozel, A., Ricard, Y., Bercovici, D., 2011. A thermodynamically self-consistent damage equation for grain size evolution during dynamic recrystallization. Geophys. J. Int. 184 (2), 719–728.
Skemer, P., Karato, S.-i., 2008. Sheared lherzolite xenoliths revisited. J. Geophys. Res.: Solid Earth 113 (B7). http://dx.doi.org/10.1029/2007JB005286. n/a-n/a, b07205.
Skemer, P., Warren, J.M., Kelemen, P.B., Hirth, G., 2010. Microstructural and rheological evolution of a mantle shear zone. J. Petrol. 51, 43–53.
Stipp, M., Tullis, J., Scherwath, M., Berhman, J., 2010. A new perspective on paleopiezometry: Dynamically recrystallized grain size distributions indicate mechanism changes. Geology 38 (8), 759–762.
Tasaka, M., Hiraga, T., Michibayashi, K., 2014. Influence of mineral fraction on the rheological properties of forsterite + enstatite during grain size sensitive creep: 3. Application of grain growth and flow laws on peridotite ultramylonite. J. Geophys. Res.: Solid Earth 119 (2), 840–857. http://dx.doi.org/10.1002/2013JB010619.
Van der Wal, D., Chopra, P., Drury, M., FitzGerald, J., 1993. Relationships between dynamically recrystallized grain size and deformation conditions in experimentally deformed olivine rocks. Geophys. Res. Lett. 20 (14), 1479–1482. http://dx.doi.org/10.1029/93GL01382.
Viegas, G., Menegon, L., Archanjo, C., 2016. Brittle grain-size reduction of feldspar, phase mixing and strain localization in granitoids at mid-crustal conditions (Pernambuco shear zone, NE Brazil). Solid Earth 7 (2), 375–396.
Warren, J.M., Hirth, G., 2006. Grain size sensitive deformation mechanisms in naturally deformed peridotites. Earth Planet. Sci. Lett. 248 (1-2), 438–450.
White, S., Burrows, S., Carreras, J., Shaw, N., Humphreys, F., 1980. On mylonites in ductile shear zones. J. Struct. Geol. 2, 175–187.